# Observation of Rubber Tire Contact Condition on Motions using Ultraviolet-Induced Fluorescence Technique

# Dissertation

Observation of Rubber Tire Contact Condition on Motions using Ultraviolet-Induced Fluorescence Technique

紫外線誘起蛍光法を用いたタイヤ転動時のタイヤゴムと路面状態の観察

Graduate School of

Natural Science & Technology

Kanazawa University

Division of Mechanical Science and Engineering

Student Number   : 1624032011

Name      : JHONNI RAHMAN

Chief Advisor    : PROFESSOR TETSUYO WATANABE

Date of Submission  : JANUARY 7, 2021

# ABSTRACT

In the study of contact mechanics between tire and road surface, the forces working on tire and road surface is divided into hysteresis and adhesive forces. The adhesive force is produced due to the interaction between rubber surface and road surfaces such as Van Der Walls force, while the hysteresis force is generated by absorbing the rebounded energy from tire rubber deformation. One way to specifically obtain the adhesive force is through measuring the contact area between tire rubber and road surface by using observation method like fluorescence microscopy. Fluorescence microscopy has some advantages that allow the researcher to visualize the contact area between mating surfaces in a very small detail and in situ. It was reported that the frictional force has linear relationship with the contact area of elastomer [1]. Due to the importance of tire rubber contact in measuring the adhesive force, this study intended to figure out the effect of external factors (such as applied load and moving speed) on the contact condition of tire rubber. This information will be very important for tire corporation in order to improve and develop superior quality of tire and also might be useful for Anti-Braking System (ABS) in vehicle.

The experiment of rubber-wheel contact area was conducted in static and dynamic conditions through in-situ observation using ultraviolet-induced fluorescence technique. This experiment carried out two types of mating contacts, flat surface of glass plate and road surface replica made of urethan material. The static contact condition was carried out on rubber-wheel to identify the applied normal load dependency on the amount of rubber-wheel contact. While the dynamic test was conducted to understand how the applied normal load and moving speed affect the contact condition of rubber-wheel. The moving speed in this study indicating a combination movement of rolling and sliding. The contact area of rubber-wheel was captured and recorded using a high-speed high speed camera. Lastly, the measurement of rubber-wheel contact area was accomplished through the utilization of analyzing software based on Otsu thresholding technique.

The experimental results describe differences in static and dynamic contact conditions based on the operating parameters. The apparent contact area fluctuation of rubber-wheel on flat surface and road surface both showed similar tendency in static condition test. Where, the contact area of rubber-wheel increased as applied normal load increased. The increasing trendline of rubber-wheel contact with both surfaces was similar to logarithmic pattern trendline, where the rise of contact area degraded at high applied normal load. Although, the

rubber-wheel contact condition in static test illustrates same tendency in both flat surface and road surface, the amount of apparent contact area was totally different. In dynamic contact, however, both rubber contact on flat surface and road surface displayed different tendency at lower moving speed dependency but similar tendency at higher moving speed.

The comparison between rubber-wheel contact on flat surface and road surface was also investigated. In stationary contact, the apparent contact area of rubber-wheel on flat surface was larger than the apparent contact area of rubber-wheel on road surface. It was because the rubber-wheel only bumped with some protrusion parts of road surface. However, the effect of applied normal load on road surface was more dominant than that on flat surface. On the other hand, the effect of moving speed on road surface was less significant compare to the apparent contact area on flat surface.

# ACKNOWLEDGMENTS

# List of contents

# List of figures

# List of Tables

# Chapter 1 Introduction

## 1.1 Background

Since decades ago, many scientists have been conducting experiment about contact mechanics of soft materials due to its significant utility in many industries. One of them is the contact condition of rubber tire of vehicles. The important roles of a tire in the vehicle system can be comprehended as its function in transmitting forces on the vehicle through tire rubber to the road in a safety manner. Therefore, traction force or grip between tire and road surface become one of the most important performance characteristics needed to understand. For example, what range of friction is needed to keep the vehicles safe when breaking or cornering, or how fast the vehicle can run to maintain safety under control. If the frictional characteristics fail, then the entire system of the vehicle will be out of control that led to car accident.

In the study of contact mechanics between tire and road surface, the forces working on tire and road surface is divided into compressive and adhesive forces. These forces help a driver to maintain the vehicles on the track safely and comfortably. The adhesive force is produced due to the interaction between rubber and road surfaces because of Van Der Walls force. As the compression force, it is generated because of the weight of vehicle and the loads inside. Many studies had established the effect of road-tire contact interaction on grip performance, noise, rolling resistance, wear, and fuel consumption, which correlates with each other [2] [3] [4] [5] [6] [7]. It was reported that 1/3 of fuel consumption is used overcome friction in vehicles. Among them 35% is used to overcome the rolling friction in the tire-road contact [7]. One way to reduce rolling resistance is by optimizing the tractional force between tire and road surface [8]. In order to optimize the tractional force, Ilse evaluated the tire and surfacing contact stresses and depth texture [3]. Bharat and Sidharth also proved in their experiment that the contact patch between tire and road surface affecting rolling resistance of vehicles [4]. Manfred Kluppel has produced a lot of articles related to contact mechanic of rubber material since decades ago. In 2008, Gert Heinrich and Manfred Kluppel had reported an article about rubber friction, tread deformation and tire traction in sliding situation [5]. Their experiment intended to contribute more data for tire dynamic contact during cornering and braking for vehicles with Anti-Braking System (ABS). All of these information imply how important the study of tire and road contact in order to solve and improve the performance of the entire vehicles.

In general, road-tire contact is highly affected by external factors such as applied load and moving speed of the vehicles. In rainy seasons for example, water on the road surface

significantly affects the grip performance of tire rubber. According to the Michelin corporation report, a tire's grip performance is reduced to 50% on a wet surface when the car runs at 60 km/h. Similarly, the tire grip coefficient, which is considered as 1 on a dry surface, is reduced to 0.6 on a wet surface with 1.5 mm depth of water when the vehicle runs at 60 km/h. The grip coefficient was 0.4 when the vehicle runs at 100 km/h, showing the effect of running speed to tire grip performance of the vehicles [6]. They also mentioned that the tire grip coefficient is highly influenced by indentation and road surface roughness. It has an undeniable relationship with the contact area between tire and road. As reported by Maegawa et.al. that the real contact area of an elastomer was linearly proportional to kinetic frictional force [1]. The information regarding the contact area is very important in designing and improving the tire's performance. Specifically, more information is needed to design a superior tire. This is can be achieved when the mechanisms of tire-road contact conditions are well understood. Moreover, a lot of data related to the contact between tire and road surface in various conditions including internal and external factors are needed. For that reason, it is essential to observe and analyze the contact condition between tire and road surface.

To understand the mechanism of tire contact and road surface, many research studies have been performed over the past several decades. In particular, the observation of soft material contact interface has been reported in several method [9] [10] [11] [12] [13] [14]. The result of these reports provided beneficial information for the improvement of the theory of soft material contacts. For example, in 1996, a group study established an experimental technique that provides high-resolution thickness measurement in the horizontal and vertical directions at 1.4 µm and 0.5 nm, respectively [14]. This technique was called relative optical interference intensity (ROII). Bongaerts et al. [12], conducted an experiment using Raman microscopy to measure fluid film thickness between rotated and pressed polydimethylsiloxane sphere on a quartz flat disc. The results showed that the contact condition varied due to sliding speed. As for fluorescence microscopy, fluorescence was first applied to tribology in the 1970s when Ford and a co-worker measured the surface film thickness of rotating cylinders and raceway using various oils [15]. The approach used depended on natural fluorescence in the oil, emitted in the visible range when excited by a mercury lamp. It was improved by replacing the mercury lamp with a He-Cd blue laser beam, leading to a longer working distance and wide range of practical applications [16]. There have been many reports on fluorescence in many studies [13]. This is because it can accurately measure the thickness between two surfaces through fluorescence light based on the actual amount of liquid within the gap. A thicker fluorescence fluid solution uses higher intensity of light emitted from the lubricant

(fluorescence solution). This happens when using the same amount of excitation energy source and concentration of fluorescence dye. The accuracy and precision of this method depend on the amount of fluorescence liquid, dye solution, and exited sources energy [17].

In this study, the contact mechanics experiment of rubber-wheel was conducted to gain a better understanding in order to contribute information for better performance of tire rubber. A rubber-wheel (same material as tire rubber) and two type of mating contacts (flat glass surface and road surface replica) were tested in both static and dynamic conditions. The static test was conducted to provide information regarding the rubber contact due to the effect of the applied normal load. While the dynamic test was meant to provide rubber contact data due to applied normal load and moving speed dependencies. The experiment was simulated under wet surface conditions. The observation method used in order to visualize the contact condition between rubber-wheel and road surface was fluorescence microscopy. In the experiment the mating surface was covered with fluorescence liquid, while ultraviolet illuminated the contact condition from below. Therefore, the observation method was named as ultraviolet-induced fluorescence microscopy.

## 1.2 Goal

The main focus on this study is to observe and to investigate the effect of applied normal load and moving speed of rubber-wheel on the contact area using fluorescence microscopy named ultraviolet-induced fluorescence technique. The specific objectives of this study are:

1. To understand the characteristics in implementing ultraviolet-induced fluorescence technique for measuring the contact area of rubber-wheel.

2. To investigate and analyze the effect of applied normal load and moving speed of rubber-wheel apparent and real contact areas on flat surface of glass plate.

3. To investigate the effect of applied load and moving speed on the apparent contact area between rubber-wheel and road surface replica.

4. To analyze the different of rubber contact between flat surface and road surface.

## 1.3 Organization of Dissertation

The content of dissertation consists of the research and experimental results during my study in Kanazawa University, Japan. There are five main parts within dissertation that describe in detail about the observation of rubber-wheel contact on running condition. The structure of dissertation is shown as follow:

- Chapter 1 is about the introduction that consists of background, goals, and structure of dissertation.

- Chapter 2 explained about the literature review that consist of tire traction, contact mechanics theory, fluorescence microcopy, Beer-Lamber law, and Otsu thresholding method.

- Chapter 3 described about the methodology. It is explained about experimental set-up, pyranine solution, experiment condition and procedure, contact area determination, image processing procedure and, about Otsu thresholding calculation using OpenCV Python.

- Chapter 4 consisted of Results and Discussion. The contents are mainly divided into four parts, they are fluorescence characteristic, rubber-wheel contact with flat surface of glass plate, rubber-wheel contact with road surface replica, and lastly the comparison between rubber-wheel contact with flat glass and road surface.

- Finally, the chapter 5 is about the conclusion and the suggestions for the future work for the improvement and better quality of this research.

# Chapter 2 Study literature

## 2.1 Tire traction

The tire roles in the vehicle system can be understood by considering the fact that every force acting on a vehicle is transmitted through its tires to the road surface. The important thing is attached to the characteristic of traction which has direct relationship to the tire. If the vehicles fail to adopt the frictional characteristic on the tire, the entire system of vehicles will be out of control which lead to the accident. Although the effect of tire fail happens in both wet and dry road surface, it much more problematic on wet surface. On wet surfaces, the effect of moving speed of vehicles become dominant which led to the significant reduction of frictional coefficient.

In actual practice, there are several factors affecting tire traction during motion. It effects on coefficient of friction are categorized in two major groups, internal factors, and external factors, respectively. The internal factors mainly related to the condition of tire itself, such as material of tire, tread pattern and so on. To improve the tire traction through this factor is by conducting experiment about the tire itself. On the other hand, the external factors are related to the condition outside the tire system such as road surface, load on the vehicles, moving speed, and temperature [17].

## 2.1.1 Internal factors

The Tread of the tire is something that every regular vehicle has on its tire. Understanding the importance of tire tread and the working mechanism of tread will help people drive safely and comfortably. Regular vehicles are designed a tire with tread to keep a vehicle running stably and safe in various condition of road surfaces. On the wet surface of road, the tread of tire has a function to squish out the water from the tire so that the tire and road surface can maintain a direct contact each other. Otherwise, the water will exist between the tire and road surface, causing the lose tire traction on the road surface. The tread pattern of rubber also allows to dig into the ground surface for better grip. In this condition tread depth can give the driver to have safer driving, better handling and cornering, and comfortable ride.

Walter E. DeVinner conducted hydroplaning test to measure the coefficient of friction of tire using four different tires, three of them were treaded tire with different pattern and the last one was smooth surface tire. As shown in *Figure 2.1*, the coefficient of friction of all treaded tires was much higher than smooth surface tire [17]. This result shows how important treaded tire for safety driving.
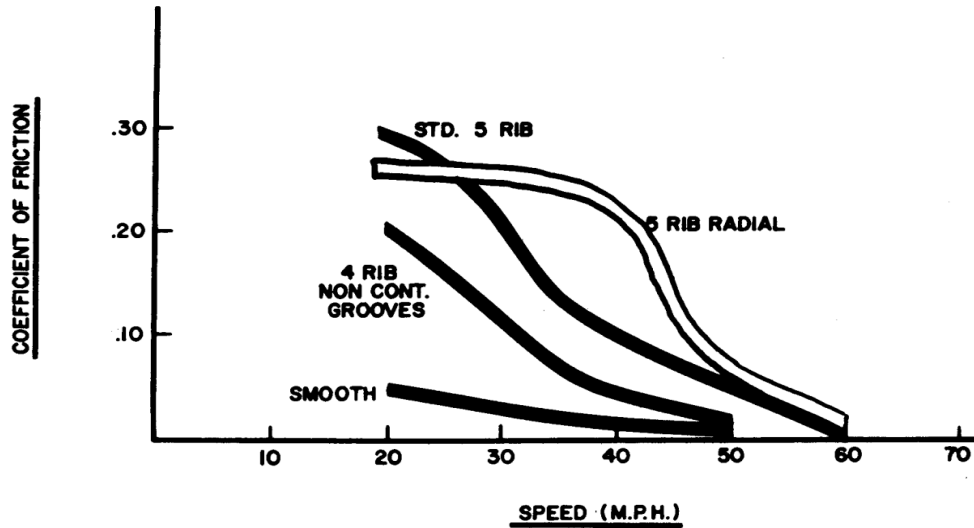
**Figure 2.1** Result of hydroplaning test on four different type of tire (standard 5 rib tire, non-continues groove tire, radial 5 rib tire and smooth surface tire) [17]

It was reported that tire construction variables have much smaller effect on the wet surface traction force. Other internal factors affect the traction force between tire and road surface is the material used on the tire, in other words the tire compound. Figure 2.2 shows the hysteresis effect on rubber due to polymer contains. The graph shows different hysteresis value obtained on different polymer contains [18].
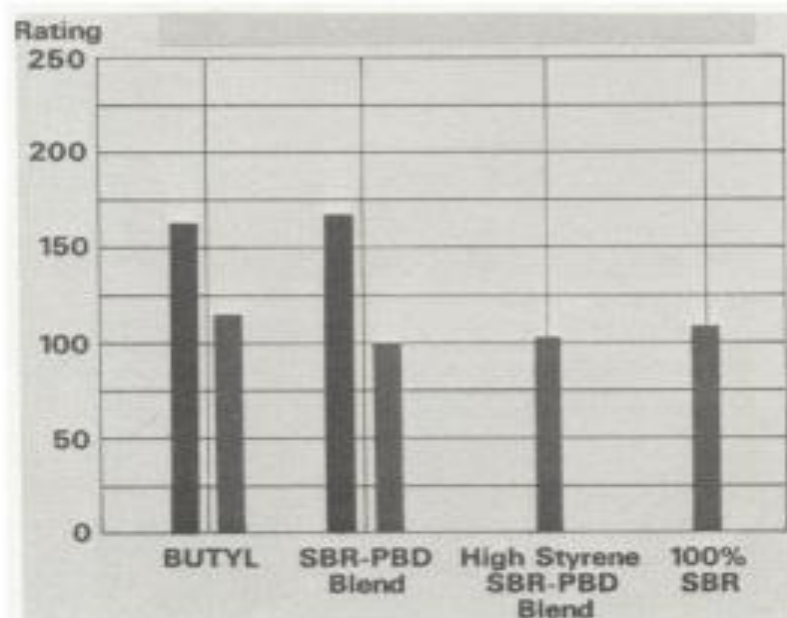


**Figure 2.2** energy absorbing characteristics (hysteresis) of different polymer contains *[18]*

6

**2.1.2** External factors

Moving speed, load, road surface, temperature, and air pressure of tire are some external factors that affect greatly on the grip performance of tire. It was reported by Binshuang et.al. that external factors mentioned above has great impact on the coefficient of friction of tire. As shown in *Figure 2.3* (a), the friction coefficient of tire increases as tire pressure increase. Same phenomena also happen for MPD values, where it increases as MPD values increase. MPD values is mean profile depth of road surface. However, moving speed of vehicles decreases the coefficient of friction of tire [19].
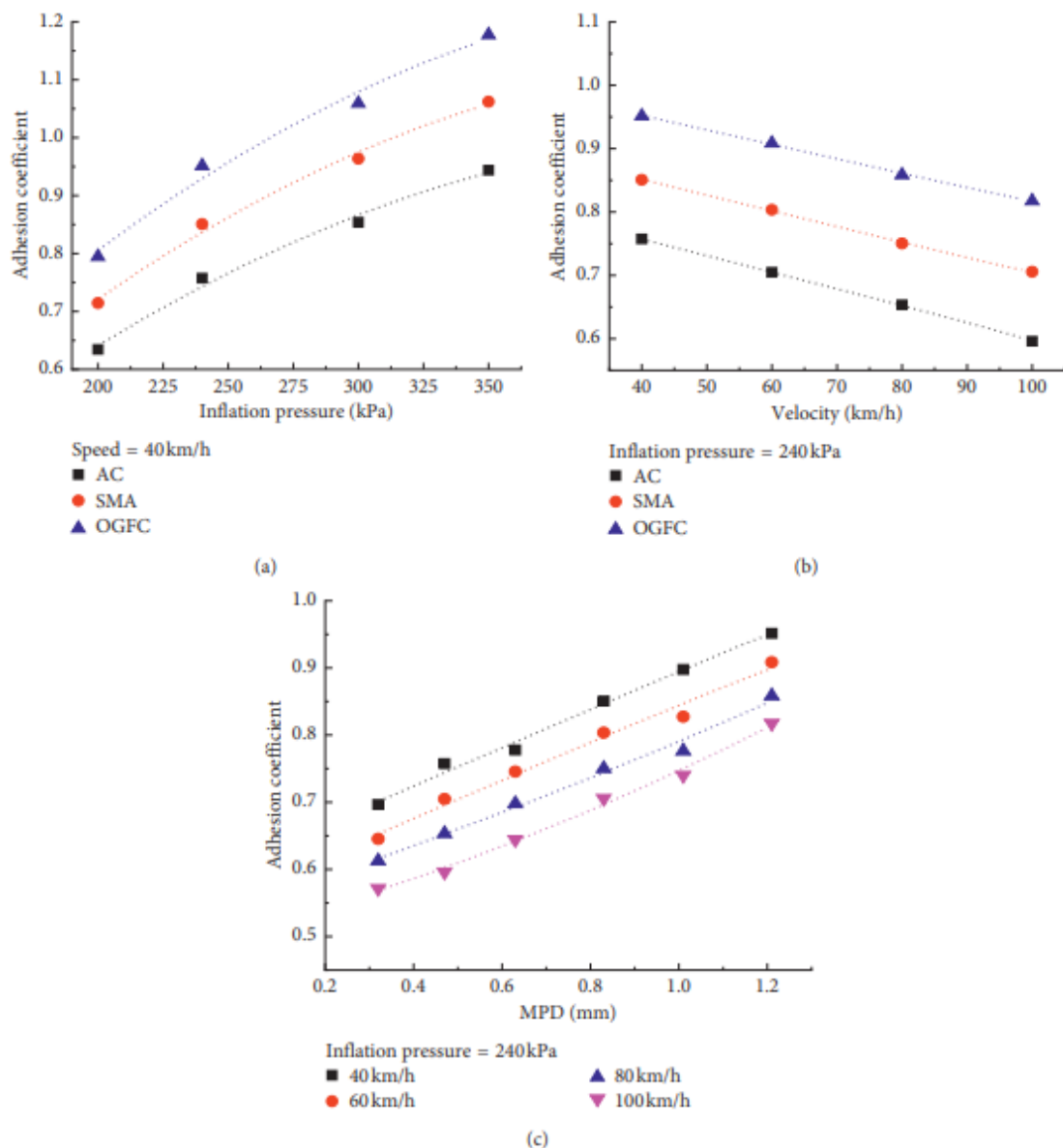


**Figure 2.3** External Influence factors analysis of the adhesion coefficient: (a)internal inflation pressure; (b) velocity; (c) MPD values [19]

## 2.2 Contact mechanic theories

The application of contact interaction in mechanics probably started firstly in 1882 by Heinrich Hertz with his publication titled "*On the contact of elastic solids*" [20]. At that time, he was working as a research assistant in the University of Berlin. His interest was aroused due to the phenomenon of elliptical pattern of contact formed between two bodies under the action of forces when he observed using interference fringes. Since then, many researchers have applied this theory to the contact of spherical surfaces. There are many famous scientists who followed the footsteps of Hertz, including Archard [21], Tabor [22], Greenwood and Williamson [23], Derjaguin BV, Muller VM, and Toporov YP (DMT) [24], and K. L. Johnson [25].

Contact mechanics is the study of solids deformation that bump each other at one or more point [25]. It is a fundamental field in tribology and generally refers to the interaction of solid surfaces. This interaction occurs on many different scales, starting from nanoscale asperities up to macroscale of tires on roads. Contacts cause huge stresses between two objects that can induce failure in the form of wear, surface fatigue and so on. Predicting these stresses is very complicated because the surface of solids is always having irregular pattern of roughness. Although many progresses have been made in solving these problems but still, there are many obstacles remain and need further analysis.

### 2.2.1 Spherical contact

The Contact mechanics theory was described by Heinrich Hertz to predict the effect of applied force on the contact area of two bodies. He found that contact area radius (a) is a function of the applied load (F), the spherical solid radius ($R^*$), and Young modulus of mating materials ($E^*$). It expressed as follows,

$$a_H^3 \approx \frac{FR^*}{E^*} \tag{2.1}$$

According to Hertz, the applied normal force (F) is proportional to displacement d, with equation can be written as follows,

$$F = \frac{4}{3} E^* R^{*\frac{1}{2}} d^{\frac{3}{2}} \tag{2.2}$$

Based on K. L. Johnson calculation, the distribution of normal pressure inside the contact area is a function of distance from the circle center of contact area that is expressed as

$$p(x) = p_0 \left(1 - \frac{x^2}{a^2}\right)^{\frac{1}{2}} \tag{2.3}$$

8

where $p_0$ is the maximum of contact pressure given as

$$p_0 = \frac{3F}{2\pi a_H^2} = \frac{1}{\pi}\left(\frac{6FE^{*2}}{R^{*2}}\right)^{\frac{1}{3}}$$

2.4

Therefore, the contact area radius can be expressed as

$$a_H^3 = \frac{3FR^*}{4E^*}$$

2.5

$R^*$ is referred to as the equivalent curvature radius of two solid spheres with different radius $R_1$ and $R_2$. $R^*$ is obtained through calculation from the following equation

$$\frac{1}{R^*} = \frac{1}{R_1} + \frac{1}{R_2}$$

2.6

Also, $E^*$ refers to the equivalent elastic Young modulus of contacting material and can be expressed as

$$\frac{1}{E^*} = \frac{1 - v_1^2}{E_1} + \frac{1 - v_2^2}{E_2}$$

2.7

where $v$ is Poisson's ratio of each solid's material.
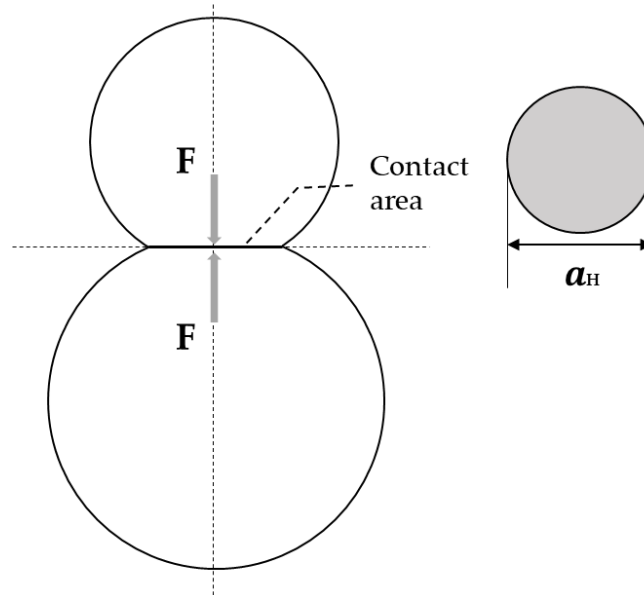


**Figure 2.4** Contact area of indented two rigid spheres

The Hertz theory described above can be used to accurately describe and satisfy the contact area of two elastic solids for non-adhesive contact. However, as adhesion forces always exist in the contact area, more precise formula for solid contact with adhesion forces included is needed.

JKR model of theory is one of the first theory that incorporate the effect of adhesion force into Hertzian contact theory. The problems aroused when some experiment showed contradicted result to the Hertz theory. As described by K. L. Johnson, K. Kendall and A. D.

Roberts [26], the Hertz theory closely fitted to experimental result at large loads. However, at low loads, they founded that the contact areas were larger than those predicted by Hertz theory and had non-zero value when the load removed. *Figure 2.5* shows the schematic model of JKR contact area.
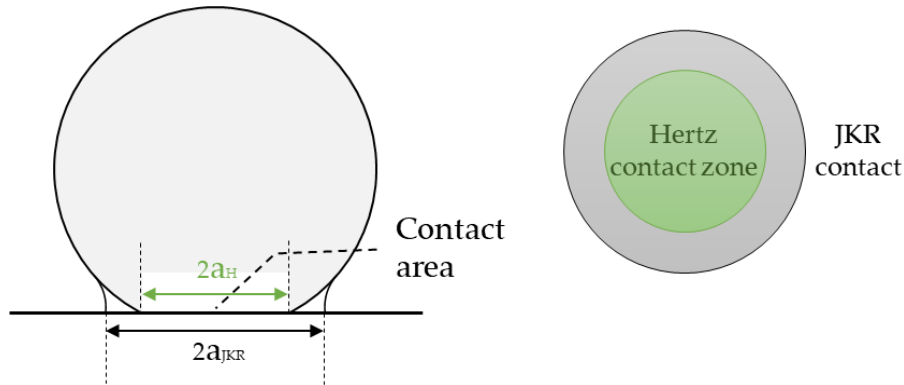


**Figure 2.5** Schematic of contact area for JKR model

According to the JKR model theory, the contact area radius as the influence of surface energy is the modification version of Hertz contact theory. It is described as

$$a_{JKR}^3 = \frac{3R^*}{4E^*}\left(F + 3\Delta\gamma\pi R^* + \sqrt{6\Delta\gamma\pi R^* F + (3\Delta\gamma\pi R^*)^2}\right)$$ 

<div align="right">2.8</div>

where $\Delta\gamma$ is the work of adhesion, which is define as

$$\Delta\gamma = \gamma_1 + \gamma_2 - \gamma_{12}$$

<div align="right">2.9</div>

when $\Delta\gamma = 0$ the JKR equation reverts to the simple Hertz equation. However, at zero load the contact area is expressed as follows,

$$a_{JKR}^3 = \frac{3R^*}{4E^*}(6\Delta\gamma\pi R^*) = \frac{9\Delta\gamma\pi R^{*2}}{2E^*}$$

<div align="right">2.10</div>

when the applied normal load is negative the contact area radius decreases. The real solution can be described as

$$6\Delta\gamma R^* F \leq (3\Delta\gamma\pi R^*)^2$$

<div align="right">2.11</div>

$$F \geq -\frac{3}{2}\Delta\gamma\pi R^*$$

<div align="right">2.12</div>

Therefore, the surfaces separation will occur when the external energy force equal to the equation shown as follow,

$$F_{JKRc} = -\frac{3}{2}\Delta\gamma\pi R^*$$

<div align="right">2.13</div>

Hence, the pull-off force is only depending on the equivalent radius of curvature and the work of adhesion, but independent to Young modulus of solids. And at critical moment of separation, the radius of contact area is expressed as

$$a_{JKRc}^3 = \frac{9\Delta\gamma\pi R^{*2}}{8E^*}$$

2.14

Other alternative theory for adhesive contact is the theory developed by Derjaguin-Muller-Toporov (DMT). DMT model theory predicts that the elastic solid contact has the same profile as Hertzian theory in addition to attractive force outside the area of contact. The schematic contact of DMT model is shown in *Figure 2.6.*
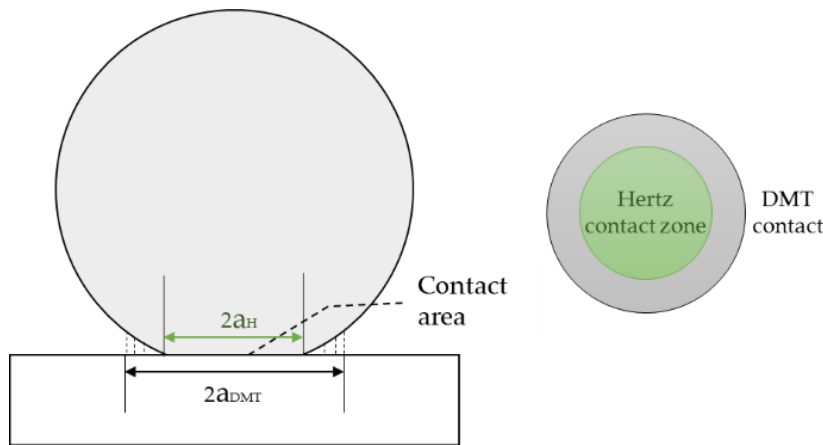


**Figure 2.6** Schematic of contact area for DMT model

According to DMT model theory, the radius of contact area between two spheres of elastic solids is described by

$$a_{DMT}^3 = \frac{3R^*}{4E^*}(F + 2\Delta\gamma\pi R^*)$$

2.15

And the pull-off force due to surface energy is shown as

$$F_{DMTc} = -2\Delta\gamma\pi R^*$$

2.16

**2.2.2** Cylindrical contact

The contact theory that has huge application on tire automobile is the contact of cylindrical solids. When a cylinder contacts with a flat surface, the contact area is initially a line until it grows and becomes a rectangle. The same situation also happens when two cylindrical solids come into contact and form a rectangular area. A cross section of contact of two cylindrical solids is shown in *Figure 2.7.*
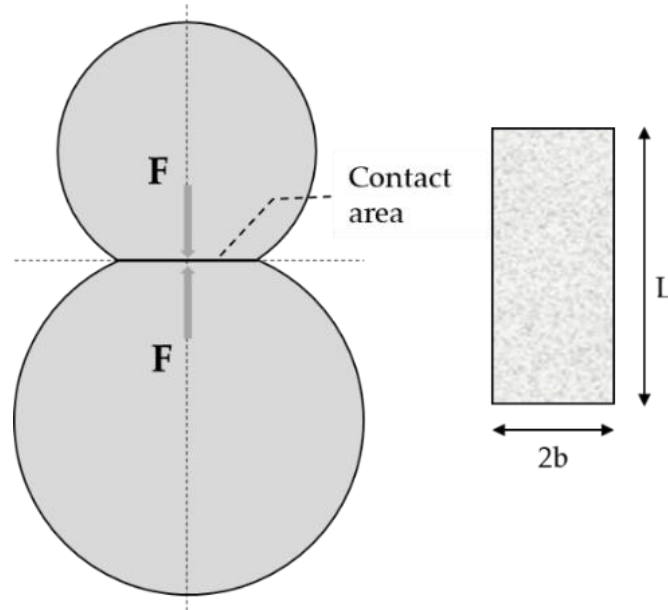
**Figure 2.7** Cross sectional of cylindrical solids contact

According to Johnson, the half contact width ($b$) of cylindrical contact is expressed as follow,

$$b^2 = \frac{4FR^*}{\pi LE^*}$$
$$\text{2.17}$$

when the cylinders come into contact, the pressure follows a parabolic profile from maximum point at the center line of contact to zero point at the edge of contact. The contact pressure for each point inside the contact area is expressed as follow,

$$p(x) = \frac{2F}{\pi bL}\left(1 - \frac{x^2}{b^2}\right)^{\frac{1}{2}}$$
$$\text{2.18}$$

and the maximum contact pressure is given by

$$P_{max} = \frac{2F}{\pi bL}$$
$$\text{2.19}$$

## 2.3 Fluorescence Microscopy

### 2.3.1 Fluorescence

The term fluorescence was stated by British scientist Gorge Gabriel Stokes (1819-1903) in his famous massive theses of more than 100 pages with the title of "On the Change of Refrangibility of light" [28]. In his theses, he used the term "*dispersive reflection*" to describe the phenomenon appeared on quinine sulphate solution. However, he said that he inclined on using the word of "*fluorescence*" instead of "*dispersive of reflection*". He noted that the fluorescence phenomenon will not occur until the solution is illuminated by ultraviolet light source (at that time he called it *darkness visible*). This observation led Him to declare that the emitting fluorescence is always have longer wavelength than the exciting light source. This transition is then being called as *Stokes Shift*, the most well-known term in photoluminescence.

There are several types of luminescence, it named according to external source of energy. When the external source of energy absorbed by a substance is light source such as infrared or ultraviolet light, this type of luminescence is called photoluminescence. In photoluminescence, when some sources of light energy are absorbed by a substance, the electron within it transit to the excitation state. Before the electron return to the ground state, some of the absorbed energy is dissipated so that the emitted light has lower energy than the absorbed light. Therefore, the emission light always has different spectrum of wavelength than the absorbed light, this is what it called as stokes shift. One of such most familiar phenomenon of photoluminescence is fluorescence, which internal energy transitions happen in a very short lifetime ($10^{-9}$ – $10^{-6}$ s). Fluorescence, therefore, decays immediately when the source of excitation light is removed.

The details energy transition process of fluorescence is shown in *Figure 2.8*. As described by Haugland (1996) [29], fluorescence phenomenon is a result of three stage processes that occurs in a fluorescence substance, named as excitation stage, excited-state lifetime, and fluorescence emission. In simple's way, excitation stage is a state when a particular light source illuminates a fluorescence substance. At that moment it excites the electron within the substance to a higher level base on the energy level of excitation light. The second stage is called excited-stated lifetime that has a very short duration of nanoseconds. The last stage is named fluorescence emission because at that stage the energy level inside a fluorescence substance return to the lowest energy level of ground state. While returning to the ground state it emits fluorescence light which has lower energy that the excitation energy level. The energy level is low because some of the energy dissipated during the excitation state.
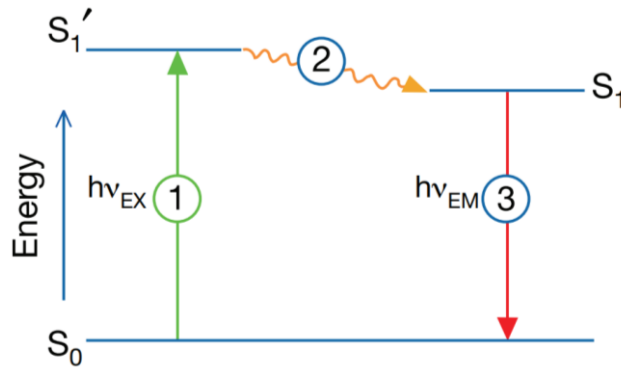
**Figure 2.8** Illustration of Jablonski diagram for
transition processes of fluorescence *[29]*

The difference between the excitation wavelength and emitted fluorescence wavelength are determined according to the type of fluorescence substance. In an experiment, fluorescence substance with a large Stokes shift is much easier and comfortable to use than the one with small Stoke shift. This is because it is very difficult to observe the emitted fluorescence light from the excitation light when there is only a slightly different between the excitation and emission wavelength. In addition, the problem of background fluorescence may occur. As an example, *Figure 2.9* shows the excitation and fluorescence spectra of nuclear dye (DAPI).
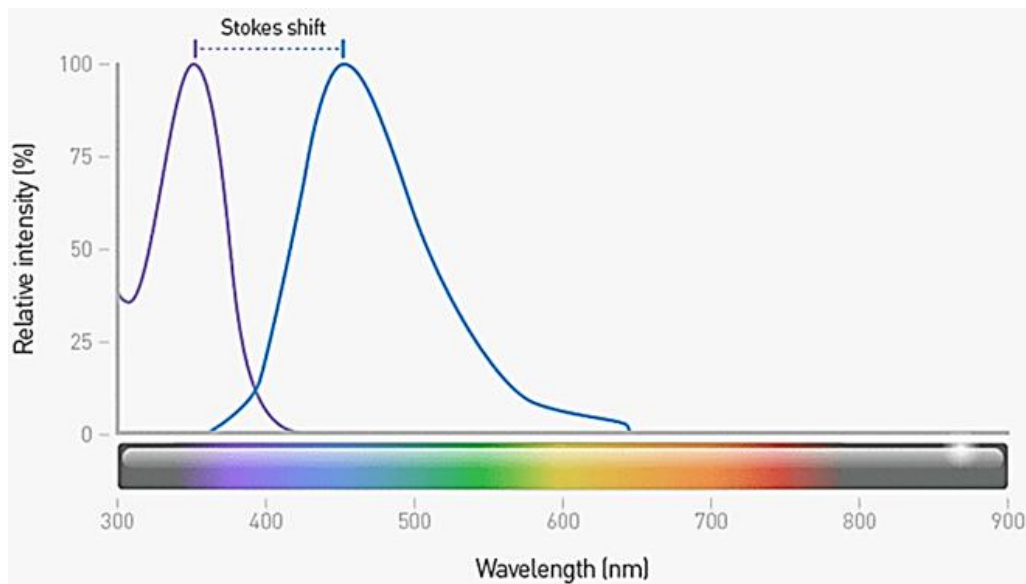


**Figure 2.9** Excitation and fluorescence spectrum of nuclear dye (DAPI) *[30]*

As described by Haugland, photo-fluorescence can be used to characterize scalar measurement on fluorescence dye solution. Fluorescence is a function of the dye characteristics, dye concentration, exciting light intensity, and so on. Once a particular dye and the concentration are selected under identical room condition, the fluorescence dependence on

these factors are constant. Other environmental parameters such as temperature and PH must also be put into consideration because its highly affect the emission of fluorescence light intensity [31].

In order to correlate two-dimensional fluorescent intensity to a scalar measurement, usually a range variation in illumination intensity must be determined. This can be achieved by using a ratio-metric technique [32]. One way to achieve this is by using two fluorescent dyes and observing the ratio of those two fluorescent dyes emissions. The emissions contain the desired scalar information as well as information on the excitation light source intensity. By observing the ratio of the emissions of each dye, variations in excitation intensity can be minimized.

**2.3.2** Fluorescence method

Fluorescence microscopy is a powerful imaging device in many field areas of study used to collect spatial and functional information on the visualized object. Fluorescence microscopy was developed by August Köhler (1866-1948) and Henry Siedentop. It was presented at the botanical institute in Vienna in 1908 through a microscopy course. The fluorescence microscopy is based on a fluorescent dye (fluorophore) contained inside the sample or individual structures. This dye is illuminated by a light source with a certain wavelength. The light source can be generated in form of a mercury-vapor lamp, LED light or a laser.

Laser Induced Fluorescence (LIF) is a typical optical spectroscopic technique where a sample is illuminated by a laser light source, and fluorescence light emitted from fluorescence sample is subsequently captured by a detector. As it implied on its name, laser induced fluorescence is a type of fluorescence microscopy that the excitation light is produced by a laser. As an analytical technique, the intensity of emitted fluorescence light is proportional to the concentration fluorophore, the intensity of excitation light and also the amount of fluorophore. Nowadays, this microscopy has become one of the most commonly use observation technique for many scientific purposes, such as medical, biological, engineering and so many other fields. LIF spectroscopy was first developed by Ricard Zare in 1968 when he conducted experiment on detecting atoms and molecules in gas phase [33].

*Figure 2.10* shows the schematic system of fluorescence microscopy. The schematic system describes the simple's setup of fluorescence microscopy with typical component consist of fluorescence dye, light source, excitation filter, dichroic mirror, emission filter and detector.

Each of these components is essential for capturing better quality of fluorescence image. *Figure 2.11* shows the image of components inside filter tube usually used in fluorescence microscopy.
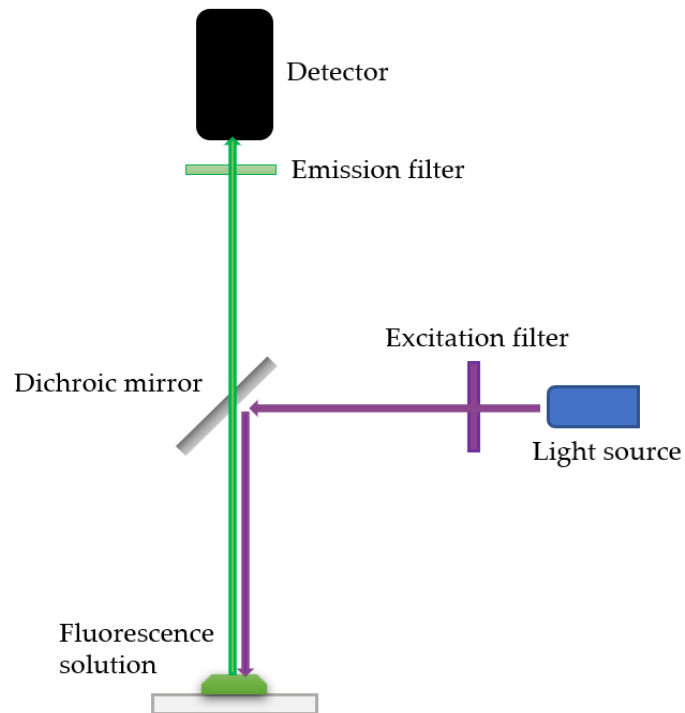


**Figure 2.10** Schematic of the working principle of fluorescence microscopy
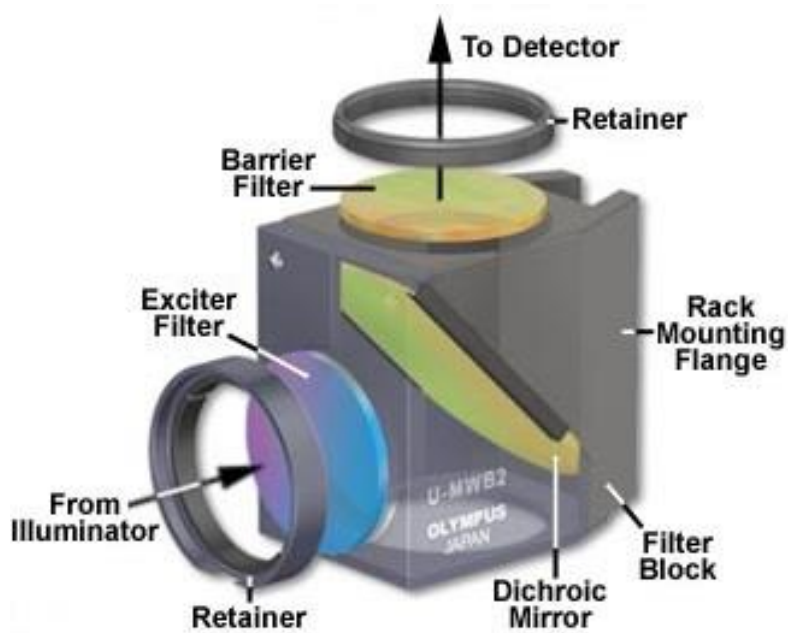


**Figure 2.11** Filter tube of fluorescence microscopy *[34]*

## 2.4 Beer-Lambert law

The law was first developed by Pierre Bouguer before 1729. It was attributed to Johan Heinrich Lambert because of his findings about path length as a variable that affect absorbance. Later, in 1852, Beer extended the experiment by adding concentration of solutions as a new parameter affecting light absorbance. Therefore, the law about light absorbance was known as Beer-Lambert law.

Lambert law reported that when monochromatic light passes through a transparent medium, the rate of decreasing intensity due to medium thickness is proportional to the intensity of the light. It means that the intensity of the emitted light decreases exponentially as the thickness of the absorbing medium increases. On the other hand, in fluorescence microscopy, the amount of fluorophore increases the emitted fluorescence intensity. Therefore, the thicker fluorescence liquid the higher intensity of emitted fluorescence intensity. However, the rate of increasing intensity is degraded at thicker fluorescence liquid. Figure 2.12 shows the sample of emitted light rate degradation due to thickness of fluorescence solution.
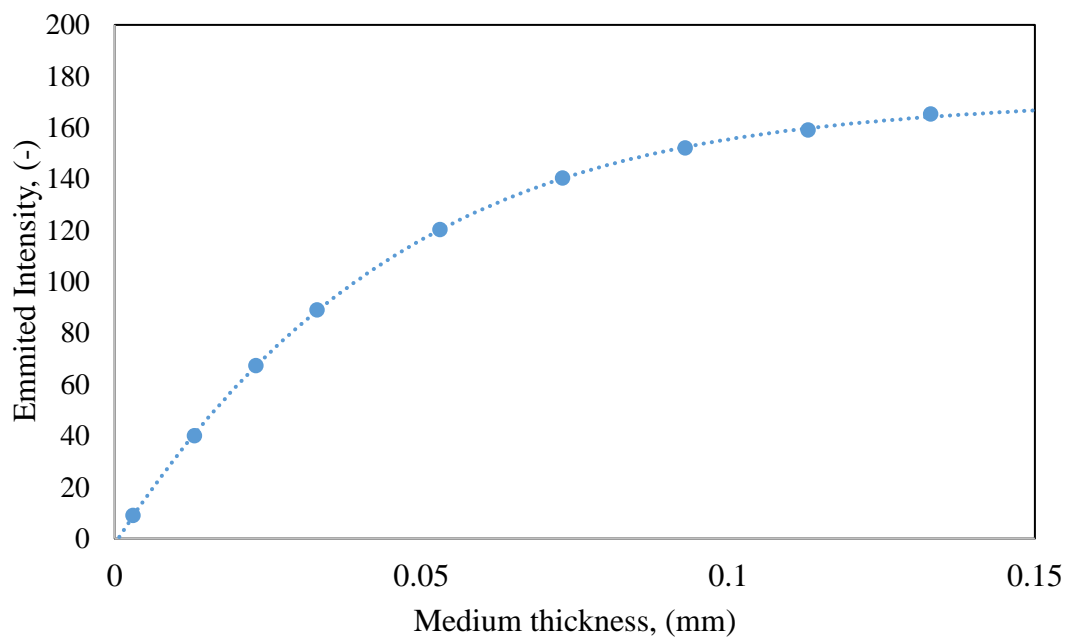


**Figure 2.12** Emission fluorescence light of pyranine solution in the function of thickness

As the explained in Lambert law, the intensity is decreasing proportional to medium thickness. Thus, the formula can be described as,

$$-\frac{dI}{dl} = al \qquad\qquad 2.20$$

Where,

I = Intensity of the incident light of wavelength $\lambda$

$l$ = Thickness of the medium

$a$ = Proportional factor

After integrating the equation 2.20, the equation can be expressed as follows,

$$\int_{I_0}^{I} -\frac{dI}{I} = a \int dl$$

$$log_e I - log_e I_0 = -al$$

$$log_e \frac{I}{I_0} = -al$$

$$I = I_0 e^{-al} \qquad\qquad 2.21$$

Later, Beer studied the effect of concentration of solution upon the absorption of light transmission. He found that it has same relationship between transmission and absorbance concentration as what Lambert discovered between transmission and medium thickness, that is the intensity of excited light decreases proportional to the increasing absorbance concentration. Thus, it can be shown as,

$$I = I_0 e^{-bc} \qquad\qquad 2.22$$

Here b is proportional factor, and c is the concentration of absorbance. From the combination of equation *2.21* and *2.22*, the following equation can be obtained.

$$I = I_0 e^{-kcl} \qquad\qquad 2.23$$

$$\frac{I}{I_0} = e^{-kcl} \qquad \text{and} \qquad \frac{I}{I_0} = 10^{-0.43\,kcl}$$

Here, 0.43 k is equal to $\varepsilon$. So, then it can be expressed as follows,

$$\frac{I}{I_0} = 10^{-\varepsilon cl}$$

$$log \frac{I_0}{I} = -\varepsilon cl \qquad\qquad 2.24$$

$$if, \quad A = -\varepsilon cl;$$

$$\because A = log \frac{I_0}{I} \qquad\qquad 2.25$$

here $\varepsilon$ = molar absorption coefficient

**2.5** Otsu Thresholding

Thresholding technique is one of the most effective and the simplest way to separate the image into two or more segmentation. The segmentation of image is a process of partitioning a digital image into meaningful multiple segments. It can be separated into multiple segments according to homogeneity criteria such as color, intensity and so on, so that it can be used to locate and identify objects and boundaries in an image [35]. As the simplest method of image segmentation through threshold value, this can convert a multilevel pixel of image into a binary image by selecting a proper thresholding value of pixel to divide image pixels into two of more different regions or objects. Thresholding generates binary images by converting all pixels below some threshold value to zero and all pixels above that threshold value into one. It is an essential and a critical step in analysis process to interpretate an image into meaning full categories. At present, image segmentation method has been implemented to various purposes such as natural images [36], topographic maps [37], satellite images [38] and medical images [39]. In the field of contact mechanic, Dina Petrova *et al*. implemented this technique to investigate the boundary threshold value to separate lubrication regimes into mixed lubrication state and hydrodynamic lubrication state [40].

Otsu thresholding method is one of the most successful methods in image thresholding with a very high accuracy. Otsu thresholding method was introduced by Japanese scholar named Nobuyuki Otsu in 1979 [41]. Otsu thresholding method involves iterating all the possible threshold value and calculating the grey pixel levels of each side between foreground and background. The fundamental idea of Otsu thresholding technique is dividing the pixels in the image into two groups with a threshold value and calculate the interclass variance between them. The aim of Otsu thresholding method is to figure out the most optimal threshold value where the sum of foreground and background (*within class* variance) is at its minimum or the calculation of *between class* variance is at its maximum. It was reported in one study that the accuracy of Otsu thresholding method through experiment using Weizmann Segmentation Database was more than 93.33% [42].

In the Otsu thresholding calculation, the grey scale of an image is assumed as $i = 0, 1, 2, …., L$. If the number of pixels at level $i$ is denoted by $n$, the total number of pixels can be expressed as $N = n_1 + n_2 +…. + n_i$.

$$N = \sum_{i=0}^{L} n_i = n_0 + n_1 + \cdots + n_L \qquad 2.26$$

The probability of grey level occurrence is calculated as,

$$p_i = \frac{ni}{N} = \frac{n_i}{\sum_{i=0}^{L} n_i} \qquad 2.27$$

The grey level can be divided into two classes, $C_0$ and $C_1$, as $C_0 = (0, 1, 2, \ldots, t)$ and $C_i = (t+1, t+2, \ldots, L)$, respectively. And the probabilities of class occurrence and the class mean levels are shown as

$$\omega_0 = Pr(C_0) = \sum_{i=1}^{t} p_i = \omega(t) \qquad 2.28$$

$$\omega_1 = Pr(C_1) = \sum_{i=t+1}^{L} p_i = 1 - \omega(k) \qquad 2.29$$

and

$$\mu_0 = \sum_{i=0}^{t} i\, p_i / \omega_0 = \frac{\mu_t}{\omega(t)} \qquad 2.30$$

$$\mu_1 = \sum_{i=t+1}^{L} i\, p_i / \omega_1 = \frac{\mu_T - \mu(t)}{1 - \omega(t)} \qquad 2.31$$

where

$$\mu(t) = \sum_{i=0}^{L} P_i, \qquad \mu_T = \sum_{i=0}^{L} iP_i \qquad 2.32$$

This is the total mean level of the original picture. For the value of t, it can be verified with the following equations:

$$\omega_0 \mu_0 + \omega_1 \mu_1 = \mu_T \qquad 2.33$$

$$\omega_0 + \omega_1 = 1 \qquad 2.34$$

The class variance is described as,

$$\sigma_0^2 = \sum_{i=o}^{t} (i - \mu_0)^2 \frac{p_i}{\omega_0} \qquad 2.35$$

$$\sigma_1^2 = \sum_{i=t+1}^{L} (i - \mu_1)^2 \frac{p_i}{\omega_1} \qquad 2.36$$

The class separability on t is shown as follows

$$\lambda = \frac{\sigma_B^2}{\sigma_W^2}, \qquad k = \frac{\sigma_T^2}{\sigma_W^2}, \qquad \eta = \frac{\sigma_B^2}{\sigma_T^2}$$

where,

$$\sigma_W^2 = \omega_0 \sigma_0^2 + \omega_1 \sigma_1^2$$

$$\sigma_W^2 = \omega_0 (\mu_0 - \mu_T)^2 + \omega_1 (\mu_1 - \mu_T)^2$$

$$\sigma_W^2 = \omega_0 \omega_1 (\mu_1 - \mu_0)^2 \qquad \text{2.37}$$

and

$$\sigma_T^2 = \sum_{i=1}^{L} (i - \mu_T)^2 \, P_i \qquad \text{2.38}$$

They are the within class variance, the between-class variance, and the total variance of levels, respectively. The threshold classes can be divided into grey levels, and this is the best threshold segmentation process.

$$\sigma_W^2 + \sigma_B^2 = \sigma_T^2 \qquad \text{2.39}$$

It shows that $\sigma_W^2$ is based on class variances (second order), while $\sigma_B^2$ is based on class means (first order). The optimal threshold t* that maximizes $\eta$, or equivalently maximizes $\sigma_B^2$ is selected by using the simple cumulative quantities.

$$\eta(t) = \frac{\sigma_B^2(t)}{\sigma_T^2} \qquad \text{2.40}$$

$$\sigma_B^2(t) = \frac{[\mu_T \omega(t) - \mu(t)]^2}{\omega(t)[1 - \omega(t)]} \qquad \text{2.41}$$

And the best optional threshold t* is the threshold value when $\sigma_B^2$ is the maximum value with criterion,

$$t^* = arg_{o \leq t < L}(max)\eta(t) \qquad \text{2.42}$$

# Chapter 3 Methodology

## 3.1 Experimental set-up

*Figure 3.1* shows the dimensions of the rubber-wheel and the assembled image of the experimental apparatus used in current study. The rubber-wheel was in the form of cylindrical with an outer diameter, inner diameter, and width of 79 mm, 41 mm, and 32 mm, respectively. The inner side of the rubber was fixed with a gear-shaped aluminum with 16 mm inner diameter. The rubber-wheel was connected to a shaft through an aluminum hole for free rotation. Also, the shaft was connected to a linear guide instrument with normal loading adjustment and flexible moving speed for dynamic condition tests. Consequently, the driving force was produced by a linear guide instrument instead of rubber-wheel rotation. *Figure 3.2* displays the mating contact materials (flat surface of glass plate and road surface replica made of urethan). The experiment using smooth surface rubber-wheel was carried out on those two type mating pairs. The road surface type used in the experiment was macro-rough and micro-rough road surface (based on Michelin report 2001), which has the best friction coefficient in damp and wet conditions [5]. During the test, the mating surfaces (flat surface and road surface) were covered by fluorescence liquid of pyranine solution representing wet conditions in the rainy season. The flat glass mating surface was known as BK7 with square shape has 100 mm in length and 5 mm thickness, respectively. The second type mating surface of road surface replica was made of urethane material. It is made in rectangular surface with 98 mm x 108 mm lengths and 37 mm of thickness. *Table 3.1, Table 3.2*, and *Table 3.3* show the specification of rubber-wheel, flat glass plate and road surface replica, respectively.



|            (a)            |            (b)            |
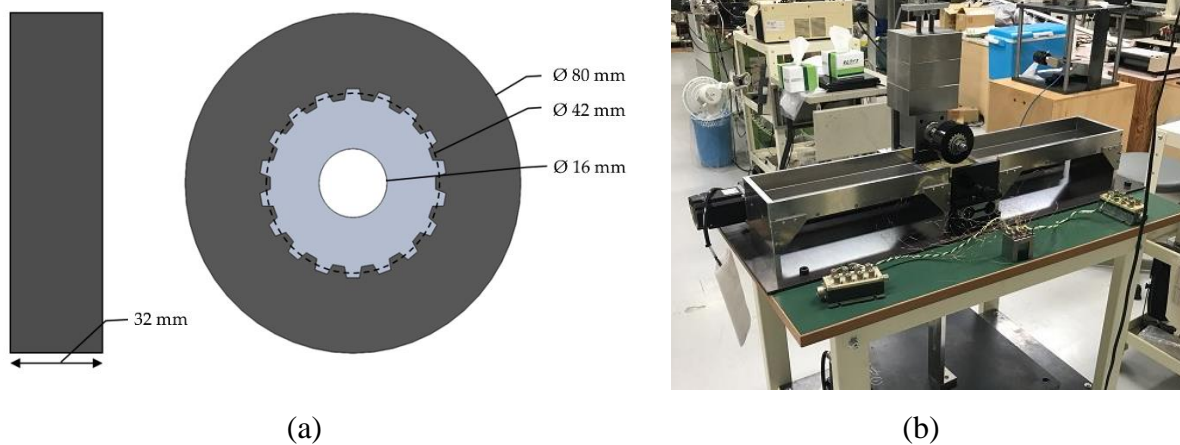
**Figure 3.1** Rubber-wheel dimensions and assembled experimental device

(a)                                                    (b)
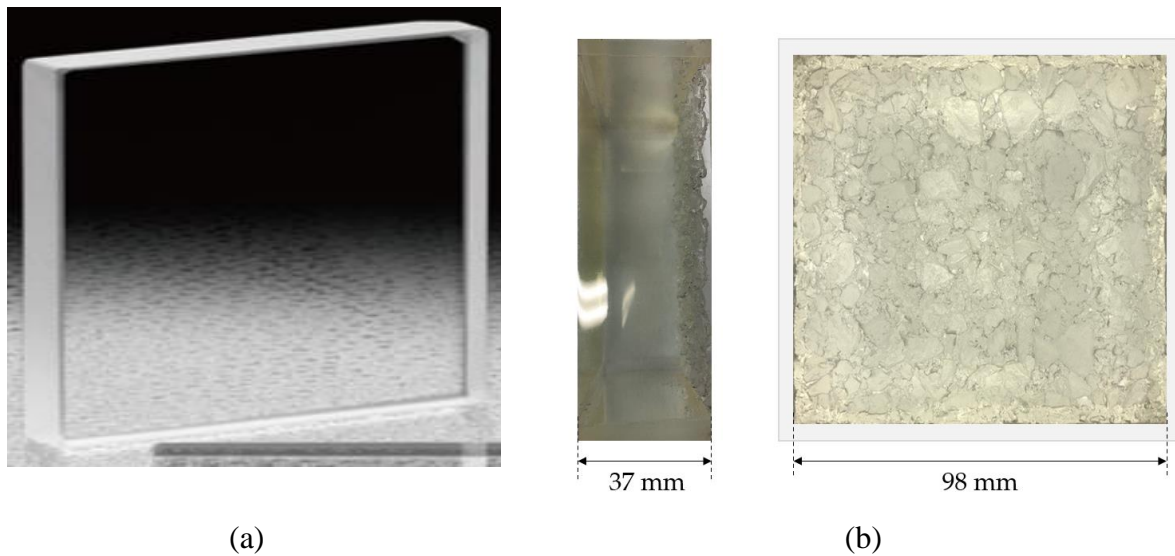
**Figure 3.2** Mating surfaces of flat glass plate and road surface replica

**Table 3.1** Specification of rubber-wheel

| Specimen | Tire rubber |
|---|---|
| Diameter, mm | ø79 |
| Width, mm | 32 |
| Poisson`s ratio | 0.49 |
| Young modulus, MPa | 2 |

**Table 3.2** Specification of glass plate

| Specimen | BK7 |
|---|---|
| Dimensions, mm | 100 x 100 x 5 |
| Density, g/cm$^3$ | 2.51 |
| Poisson`s ratio | 0.206 |
| Young modulus, MPa | 82 x 10$^3$ |
| Refractive index | 1.53627 (365 nm) |
| Internal transmittance | 0.988 (365nm) |

**Table 3.3** Specification of road surface replica

| Specimen | Urethan |
|---|---|
| Dimensions, mm | 98 x 108 x 37 |
| Density, g/cm$^3$ | 2.51 |
| Poisson`s ratio | 0.35 |
| Young modulus, MPa | 200 |

23

In this apparatus, the contact area was observed using a high-speed digital camera (HAS-U2; DITECT, Ltd, Japan) with an adjustable gain number and image size. The camera produces a maximum of 7500 frames per second (fps) for recording images of high-speed movement. *Figure 3.3* shows the image of high-speed camera used in this study, while the detail information about the camera shown in *Table 3.4*. The excitation light source was provided by ultraviolet (U.V.) light with a 365nm peak of wavelength. The apparatus mechanism was differed from the commonly use laser-induced fluorescence (LIF), which uses a half or dichroic mirror to reflect the light source perpendicular to the observing surface. The current experiment utilized a ring-shaped U.V. device as a light source for excitation, located beneath the road replica. The dichroic filter and high speed camera were placed below the U.V. light source. This way enables high speed camera to directly capture the image of contact between rubber-wheel and mating pairs without utilizing a half-mirror or dichroic mirror. Also, the working distance of the high speed camera and rubber-wheel contact can be modified as desired based on a wide range of the image. The green-dichroic-filter (passing wavelength between 505nm and 575nm) was placed on the top of the camera to capture the only green color of fluorescence light for analysis. Hence, this apparatus enables us to conduct an experiment for in-situ observation and measure a wide range of contact area. The captured images were then recorded to P.C. for further analysis. The detailed outline of the observation system is shown in *Figure 3.4*.



**Figure 3.3** High-Speed Digital Camera [43]

**Table 3.4** High-speed digital camera specifications *[43]*

| Camera | Specification |
| --- | --- |
| Camera type | Mono (HAS-U2M) |
| | Color (HAS-U2C) |
| Sensor type | CMOS |
| A / D | 10bit |
| Max. resolution | 2592 x 2048 (5 M Pixel) |
| Memory size | 2 GB |
| Shutter (exposure) | Minimum 1/100,000 (10 $\mu$) |
| Frame per second | 60 – 7500 fps |
| Sensitivity (at 550nm) | 7.5 V / lux. s |
| Weight | Approximately 210 g. |
| Size | 44 mm x 44 mm x 81.5 mm |
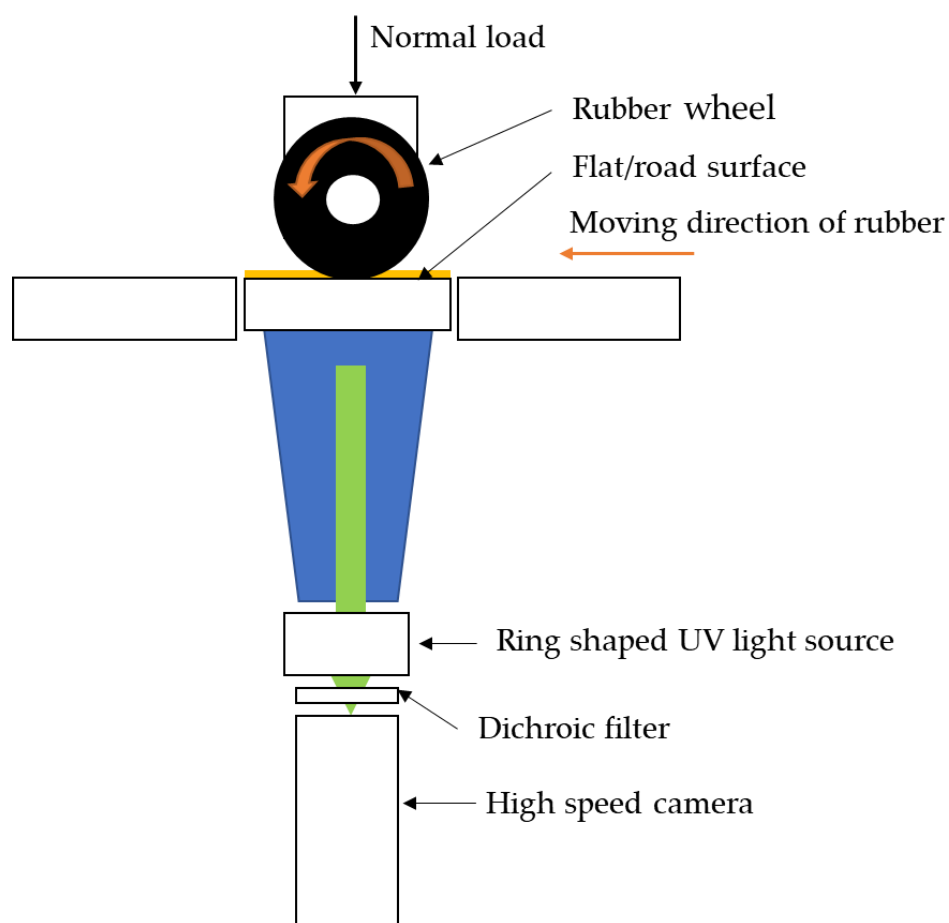


**Figure 3.4** Schematic outline of ultraviolet-induced fluorescence microscopy

## 3.2 Pyranine Solution

One of the easily found fluorescence compounds is pyranine, which has chemical composition of $C_{16}H_7Na_3O_{10}S_3$ and 524.39 g/mol molecular weight. *Figure 3.5* shows the images of pyranine compound and mixed-pyranine substance in destillated water (pyranine solution), as detail information about fluorescence compound shown in *Table 3.5*. The main reason pyranine dye was chosen for this study is because of its superiority of having large gap wavelength between the excited of UV light source and emitted pyranine-dyed-fluorescence light. It makes easy for researchers to confirm and differentiate all parts of contact area and non-contact area by observing the existence of pyranine solution inside the contacting parts. Moreover, with the excellence characteristic of ultraviolet that is invisible light make it more convenience in observing contact condition. Because of these properties, a part of observing contact area, pyranine solution also used in many other purposes such as pH indicator [44], tracer agent and so on.

This study utilized U.V. light with a peak wavelength of 365 nm as an excited energy source to illuminate pyranine liquid solution (mixed pyranine dye within pure water). As the U.V. light which is invisible to the human eye, is absorbed by pyranine solution, it then releases visible region of spectrum (green light) with a peak wavelength of 513 nm. Pyranine fluid solution emits fluorescence intensity does not only depend on dye concentration, amount of lubricant, and excited source, but also depend on salt and PH contain within the fluid solution [31] [45] [46]. Because of these dependencies the experiment was carried out in the same parameters, so that the emitted fluorescence intensity only indicating the existence of fluorescence liquid (which differentiate the contact area and non-contact areas).



**Figure 3.5** Images of pyranine substance and solution

**Table 3.5** Specification of pyranine substance

| Substance | Pyranine |
|---|---|
| Chemical formula | $C_{16}H_7Na_3O_{10}S_3$ |
| Molecular weight, g/mol | 32 |
| Appearance | Yellow-green crystalline powder |
| Fluorescence peak wavelength, nm | 513 |

## 3.3 Experimental condition and procedure

The rubber-wheel contact was captured and recorded using the high-speed high camera under stationary and dynamic conditions. As shown in *Table 3.6*, the stationary test was conducted by pressing the rubber-wheel with several variant of normal loads, ranging from 40.2 N to 157 N. As the rubber-wheel material kept deforming during pressing (called creep deformation), rubber creep experiment was conducted to obtain the selected pressing time in which the creep deformation was minimal so that it can be ignored. *Figure 3.6* shows the deformation of the rubber-wheel contact area caused by 40.2 N load, with over 600 seconds of pressing time. The result shows that the appropriate pressing time was 300 seconds, beyond that pressing time the deformation of the rubber-wheel contact area was very minimum. The same pressing time was adopted by Satoru et al. when conducting a stationary test to measure the real contact area [47]. Therefore, the rubber-wheel contact area of the experiment on the static test was maintained for 300 seconds before the image was captured. After the contact image captured, the rubber-wheel was removed from the mating surfaces for about 300 seconds before conducting the next test to ensure the rubber-wheel returned to its initial condition.

On the dynamic condition test, a loaded rubber-wheel was running on the top of fluorescence-liquid-covered mating surfaces with a constant moving speed of 2, 4, 8, 20, 40, 80, and 160 mm/s, respectively. These 7 different moving speeds were conducted as one set. Every set of dynamic tests was performed under 5 variant applied loads of 40.2, 60.8, 80.4, 99, and 121.5 N, respectively. In this study, the moving speed representing free rotation which is a mixed movement of rolling and sliding. The information on the applied load and moving speed in the dynamic test is shown in *Table 3.7*. The contact areas during movement were captured at 100 frames per second (fps) and a shutter speed of 1/200. The detailed information of high speed camera specifications is shown in *Table 3.8*.

**Table 3.6** Experimental conditions for static contact

| Contact condition | Applied load (N) |
|---|---|
| Static contact | 40.2 |
| Static contact | 50.0 |
| Static contact | 59.8 |
| Static contact | 69.7 |
| Static contact | 80.4 |
| Static contact | 90.3 |
| Static contact | 99.1 |
| Static contact | 121.5 |
| Static contact | 140.3 |
| Static contact | 157 |
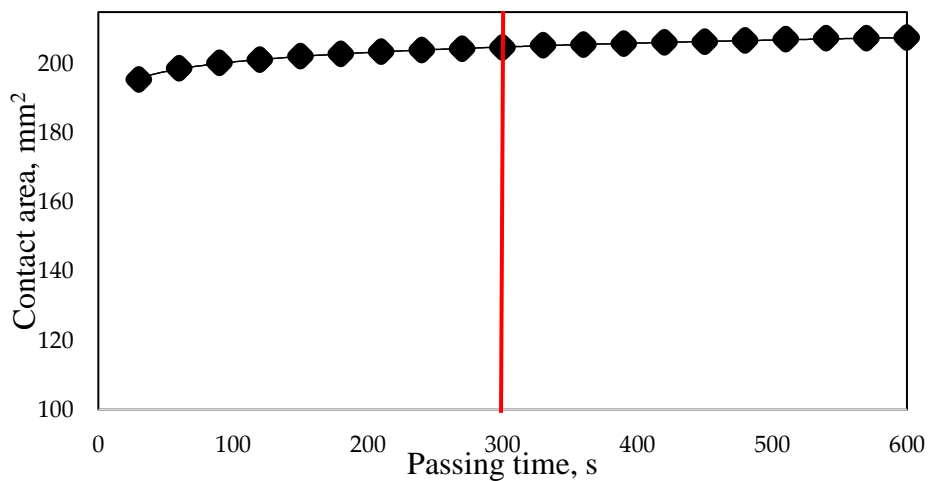


**Figure 3.6** Rubber-wheel deformation due to elapsed time

**Table 3.7** Experimental condition for dynamic condition contact

| Contact condition | Applied load (N) | Moving speed (mm/s) |
|---|---|---|
| Dynamic contact | | 2 |
| Dynamic contact | 40.2 | 4 |
| Dynamic contact | 60.8 | 8 |
| Dynamic contact | 80.4 | 20 |
| Dynamic contact | 99 | 40 |
| Dynamic contact | 121.5 | 80 |
| Dynamic contact | | 160 |

**Table 3.8** Specification of the captured image

| Camera | CCD camera |
|---|---|
| Field of view, mm | 40 x 30 |
| Number of pixels, pixels | 1600 x 1200 |
| Frame rate, fps | 100 |
| Shutter speed, | 1/200 |

The temperature of the dye solution has huge impact on fluorescence intensity [48]. Therefore, all experiments were performed in an air-conditioned room with temperature and humidity set at approximately 23 $^{\circ}$C and 65 %, respectively. Also, the distilled water used for the pyranine solution came from the same source with constant density and P.H.

## 3.4 Contact area determination

As the experiment used optical measurement method such as fluorescence microscopy, there are some factors affecting the intensity on contact condition such as light reflection and scattering light, as well as the impurity inside the material. Consequently, it was difficult to directly identify the contact region based on fluorescence intensity only. There is currently no method to determine the correct boundary of the apparent or the real contact areas other than using the thresholding number. According to several studies, the Otsu thresholding method is the best method in deciding the most appropriate thresholding number for image analysis. It was reported that the accuracy of the Otsu thresholding method through an experiment using the Weizmann Segmentation Database was more than 93% [42]. In line with this, the current study used the Otsu thresholding method to determine the boundary for the apparent contact area of rubber-wheel and road surface replica. The same way also goes for rubber-wheel contact with flat surface.

Despite its excellency in determining thresholding value, the Otsu method cannot directly be used on rubber-wheel contact on road surface replica. This is because the irregular pattern of the road surface disturbs the calculation of determining thresholding value. Fortunately, there is no problems in determining Otsu thresholding value on rubber-wheel and flat surface contact. In the Otsu thresholding method, all image information is recognized as essential data to be calculated. It cannot be explicitly classified into intended information with many variables on the image. As shown in *Figure 3.7* (b), the binary image based on the Otsu thresholding method for road surface and rubber-wheel does not only displayed the contact region, but also non-contact region of rubber-wheel contact due to the complex pattern of road

surface. Therefore, the thresholding value for road surface replica was decided based on rubber-wheel contact on the flat surface of same material (urethane) with identical dimensions and properties. *Figure 3.8* shows the image of rubber-wheel contact on a flat surface of urethane material and its binary image. The value produced using the Otsu thresholding method for the apparent contact area was 36. Accordingly, this thresholding value was used as boundary thresholding value to measure the apparent contact area of rubber-wheel and road surface. *Figure 3.9* shows the image of rubber-wheel contact on a road surface and the binary images of the apparent contact area based on the Otsu thresholding method. The binary image in *Figure 3.9* (b) and (c) display only the apparent contact area of rubber-wheel and road surface. The following experimental data of the apparent contact area between rubber-wheel and road surface replica was measured based on a thresholding value of 36. *Figure 3.10* shows the image and plot profile of road surface contact with rubber-wheel. Red line indicating the measured position on rubber-wheel contact.
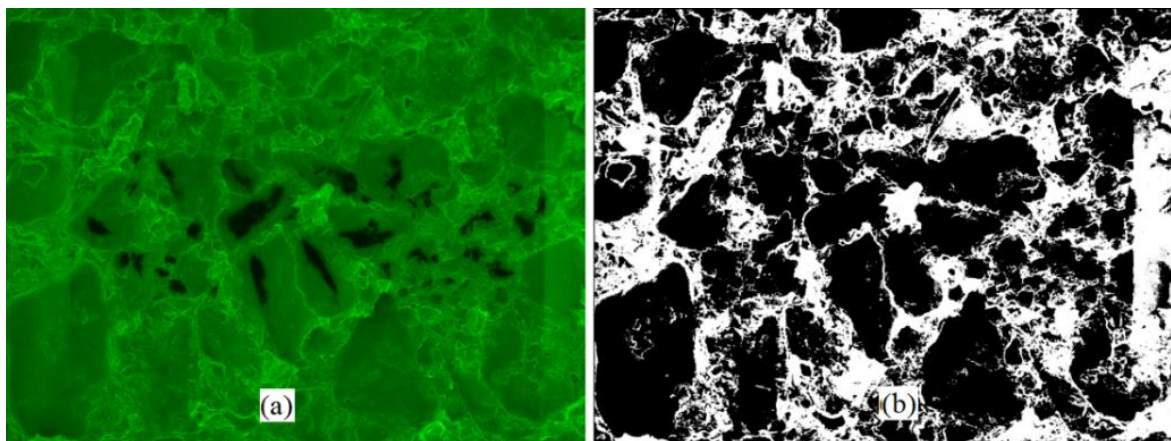


**Figure 3.7** Rubber-wheel contact on road surface of urethane material under normal load 40.2 N, (a) original image; (b) binary image based on Otsu thresholding
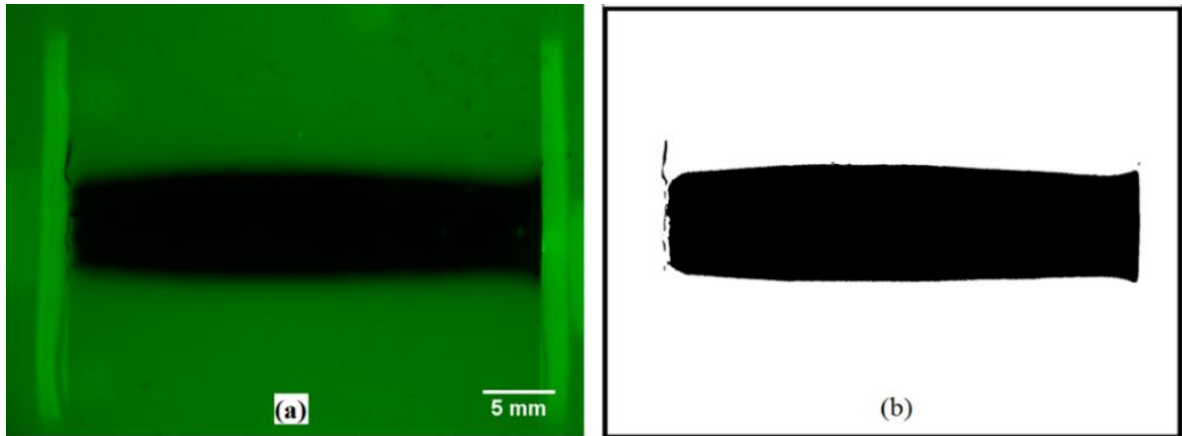
**Figure 3.8** Rubber-wheel contact on the flat surface of urethane material under normal load 40.2 N, (a) original image; (b) binary image based on Otsu thresholding
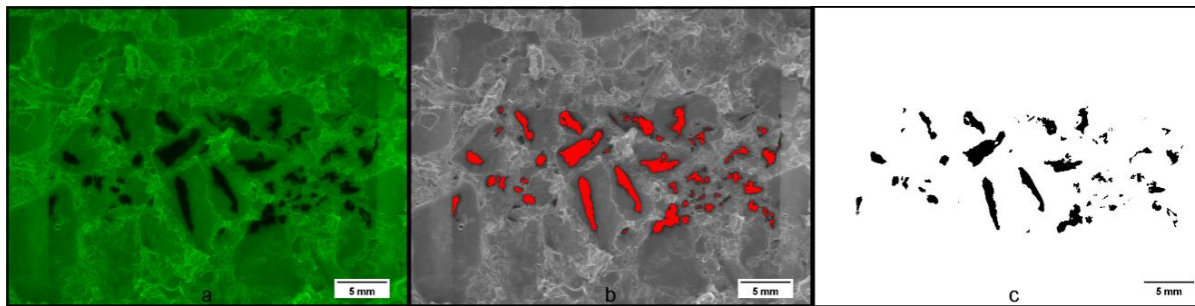


**Figure 3.9** Binarization image of rubber contact on road surface replica under 80,4 N applied load: (a) original image, (b) red binary with road replica background, (c) black and white binary image
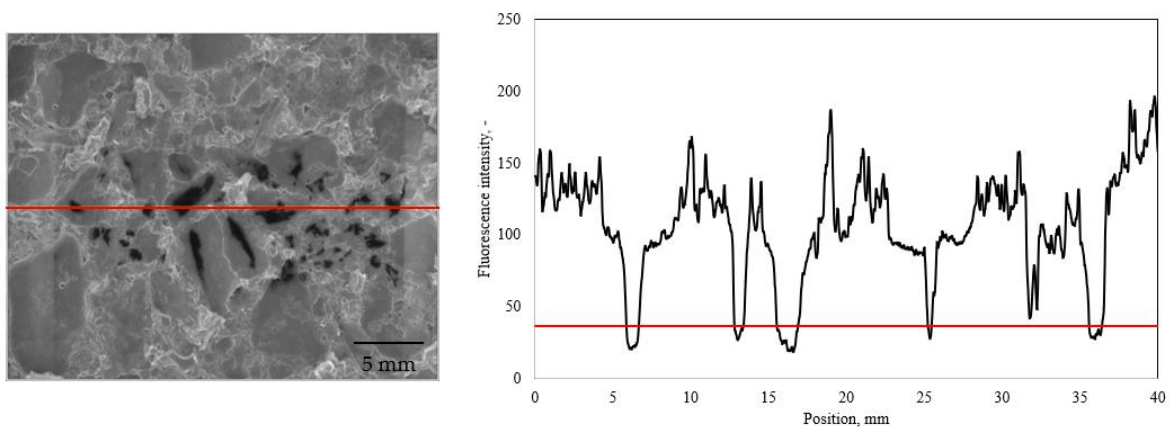


**Figure 3.10** Fluorescence image and the plot profile of rubber-wheel contact on road surface

In case of contact between rubber-wheel and flat surface, since the impurity inside the glass and the captured parameters were different compare to urethan material, the Otsu thresholding value was calculated separately. The boundary of apparent contact area of rubber-wheel calculated using Otsu method formula for our captured condition was at threshold value 38. Consequently, the intensity of 38 and below was considered as the apparent contact area of rubber-wheel and flat surface, while above that value was regarded as non-contact region. *Figure 3.11* shows the image of rubber-wheel contact on flat surface and its binary image of contact area using thresholding number 38.



5 mm
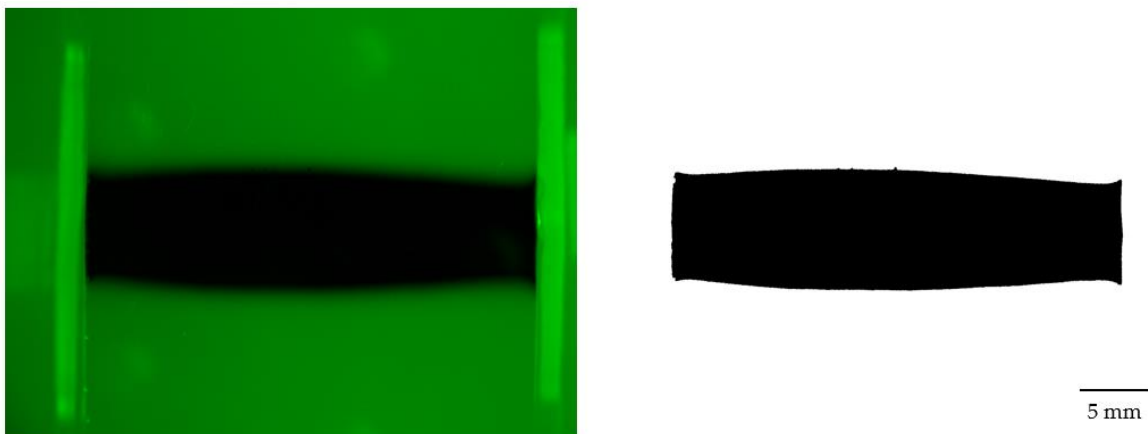
**Figure 3.11** Original and binary image of rubber-wheel contact on smooth flat surface under 80.4 N applied normal load

In case of real contact area, it can only be determined on rubber-wheel contact on flat surface as the real contact condition is confirmed within the rubber contact where contact pressure applied. Theoretically the intensity within contact pressure is zero. However, due to the effect of scattering light, the intensity within the contact pressure was not zero. It varied slightly based on the intensity of excitation light used for illumination. Therefore, the boundary value of real contact area was decided based on the fluorescence intensity within the contact pressure. The boundary value displayed on plot profile of rubber-wheel contact on flat surface as shown in *Figure 3.12* was 4. Thus, the intensity below 4 is recognized as the real contact region of rubber-wheel on flat surface.
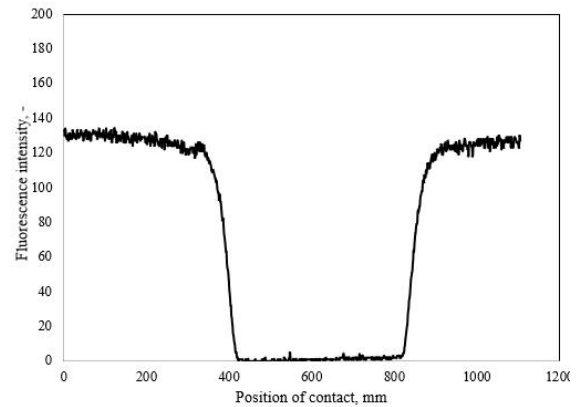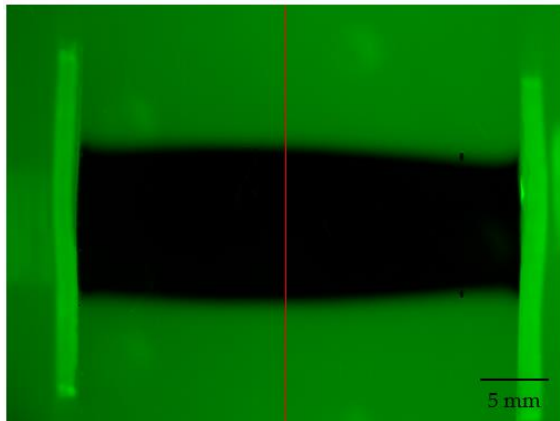
**Figure 3.12** Fluorescence image and plot profile of rubber-wheel contact on flat surface (the image belongs to applied load 157 N)

However, the same method cannot be applied for rubber-wheel contact on road surface. Due to the complexity of irregular road surface pattern, the real contact condition cannot be identified the same way as rubber-wheel contact on flat surface. The interference occurs on road surface more complicated, not only scattering light but also mainly affected by reflection that happen due to irregular pattern of surface. Currently there is no method can be used to confirm the real contact area of road surface.

## 3.5 Image processing procedure

Processing procedure for contact area measurement are described as follows (see *Figure 3.13*),

1. Open ImageJ
2. Open file to analyze **Menu bar** > **File** > **open**
3. Splitting image into RGB (Red, Green, Blue) color images, and then use green color image for further processing **Menu bar** > **Image** > **Color > Split channels**
4. Real Contact Area **Menu bar** > **Image** > **Adjust > Threshold**
5. Insert threshold value to make binary image of real contact area**.**
6. To measure the real contact area **Menu bar > Analyze > Analyze particles**
7. The analyze information including real contact area written on summary table
8. Record the real contact area and save the binary image.
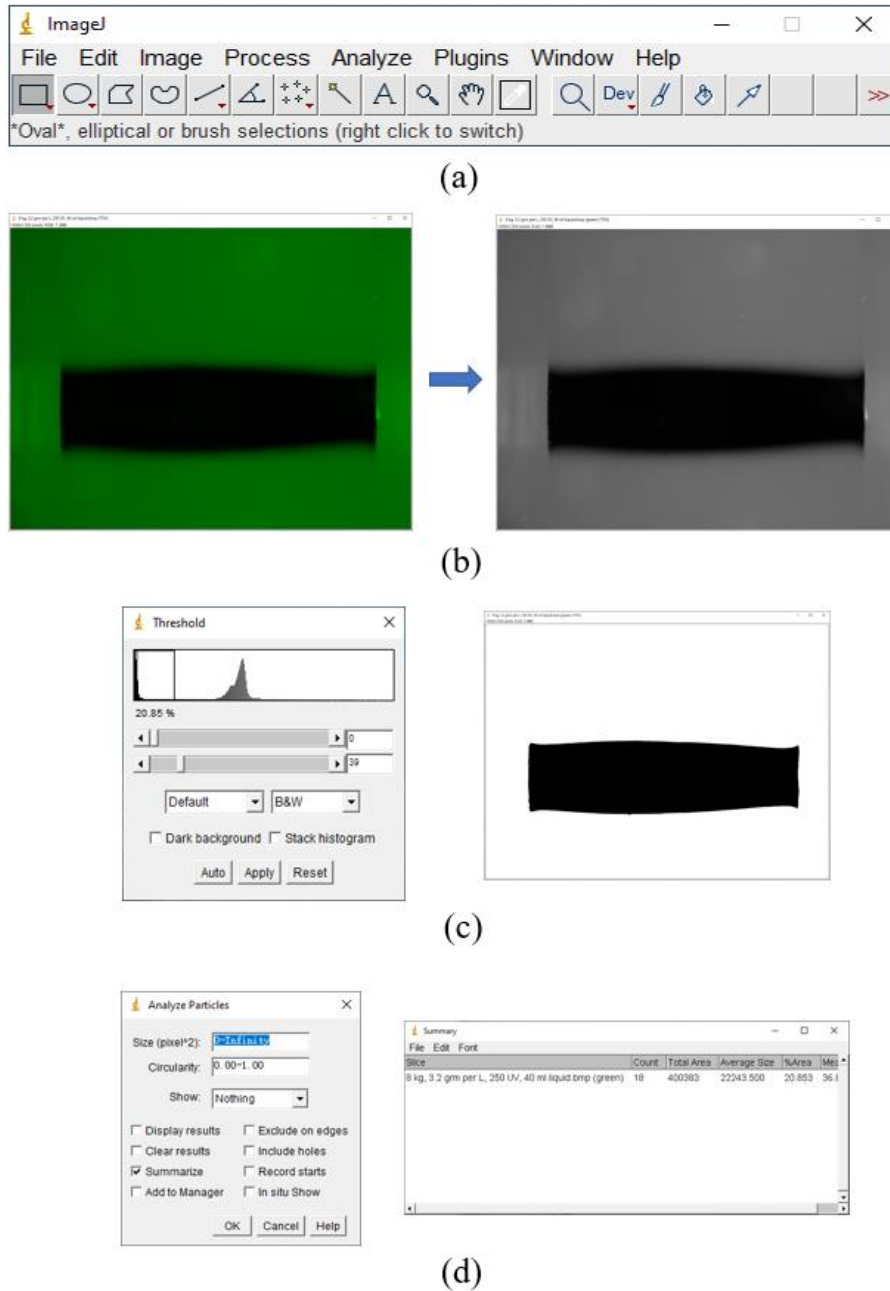
**Figure 3.13** Image processing (ImageJ) working flow of contact area identification: (a) Menu bar, (b) Color splitting, (c) Threshold adjustment for binary image, (d) Analyze particle for detail information

The processing procedure to obtain plot profile data are shown as follows (see *Figure 3.14*),

1. Open ImageJ
2. Open file to analyze **Menu bar** > **File** > **open**

3. Splitting image into RGB (Red, Green, Blue) color images, and then use green color image for further processing **Menu bar** > **Image** > **Color > Split channels**

4. Remove noise **Menu bar > Process > Noise > Despeckle**

5. Select line on menu bar and draw line needed to be measured**.**

6. To measure the real contact area **Menu bar > Analyze > Plot Profile**

7. On plot profile table **More > Copy all data**, then paste it on Microsoft excel for further analysis.
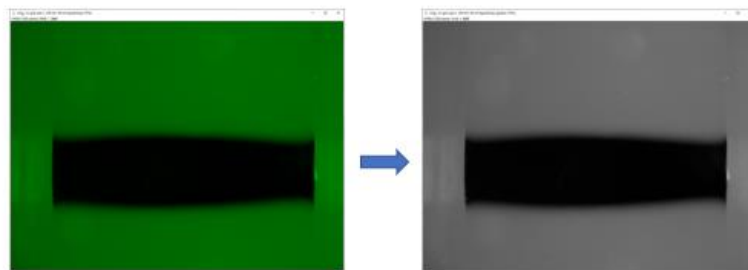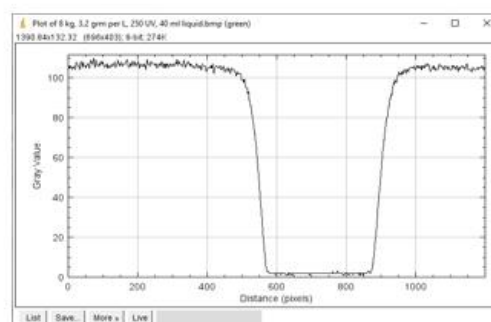


**Figure 3.14** Image processing (ImageJ) working flow of plot profile making: (a) Menu bar, (b) Color splitting, (c) Line on image, (d) Plot profile graph

## 3.6 Otsu thresholding calculation using OpenCV Python

OpenCV python was used to calculate thresholding value of Otsu thresholding. The formula programming for this calculation is shown as follow [49].

```python
import cv2 as cv
import numpy as np
from pip._vendor.msgpack.fallback import xrange

img = cv.imread('contact image.png',0)
blur = cv.GaussianBlur(img,(5,5),0)
                                    # find normalized_histogram, and its cumulative distribution
function
hist = cv.calcHist([blur],[0],None,[256],[0,256])
hist_norm = hist.ravel()/hist.sum()
Q = hist_norm.cumsum()
bins = np.arange(256)
fn_min = np.inf
thresh = -1
for i in xrange(1,256):
    p1,p2 = np.hsplit(hist_norm,[i])          # probabilities
    q1,q2 = Q[i],Q[255]-Q[i]                   # cum sum of classes
    if q1 < 1.e-6 or q2 < 1.e-6:
        continue
    b1,b2 = np.hsplit(bins,[i])                # weights

    # finding means and variances
    m1,m2 = np.sum(p1*b1)/q1, np.sum(p2*b2)/q2
    v1,v2 = np.sum(((b1-m1)**2)*p1)/q1,np.sum(((b2-m2)**2)*p2)/q2

    # calculates the minimization function
    fn = v1*q1 + v2*q2
    if fn < fn_min:
        fn_min = fn
        thresh = i

# find otsu's threshold value with OpenCV function
ret, otsu = cv.threshold(blur,0,255,cv.THRESH_BINARY+cv.THRESH_OTSU)
print( "{} {}".format(thresh,ret) )
```

**Figure 3.15** Otsu thresholding value identification program on OpenCV

# Chapter 4 Results and discussions

## 4.1 Fluorescence characteristic

**4.1.1** The effect of U.V. light source intensity

As the intensity of fluorescence light is directly affected by the intensity of U.V. light source, the intensity of U.V. light characteristic was investigated. The U.V. light device used in the current study is adjusted in five different intensity. *Figure 4.1* shows the captured fluorescence image which was illuminated on 25 mg/L pyranine solution on the top of flat surface glass plate using 1700, 3400, 5100, 6800 and 8500 $\mu M/cm^2$ five different U.V. light source intensities respectively (the image belongs to 8500 $\mu M/cm^2$ U.V. light source). The orange line is the measurement position of plot profile for every images. The measured result of plot profile was shown in *Figure 4.2*, while the relationship between fluorescence intensity and UV light sources intensity was shown in *Figure 4.3*. The result shows that fluorescence intensity increased linearly as UV light sources intensity increased. This means fluorescence intensity captured by high speed camera was proportional to the U.V. light source intensity in linear multiplication. Therefore, the selection of UV light intensity for microscopy experiment can be adjusted based on the purpose of measurement and the amount on fluorescent liquid used in the experiment. As for current study, since the purpose was to investigate the contact area between rubber-wheel and mating contacts, the intensity which is very sensitive to the smallest amount of pyranine solution was used. For this purpose, the maximum intensity of U.V. light source was implemented. It was 8500 $\mu M/cm^2$.
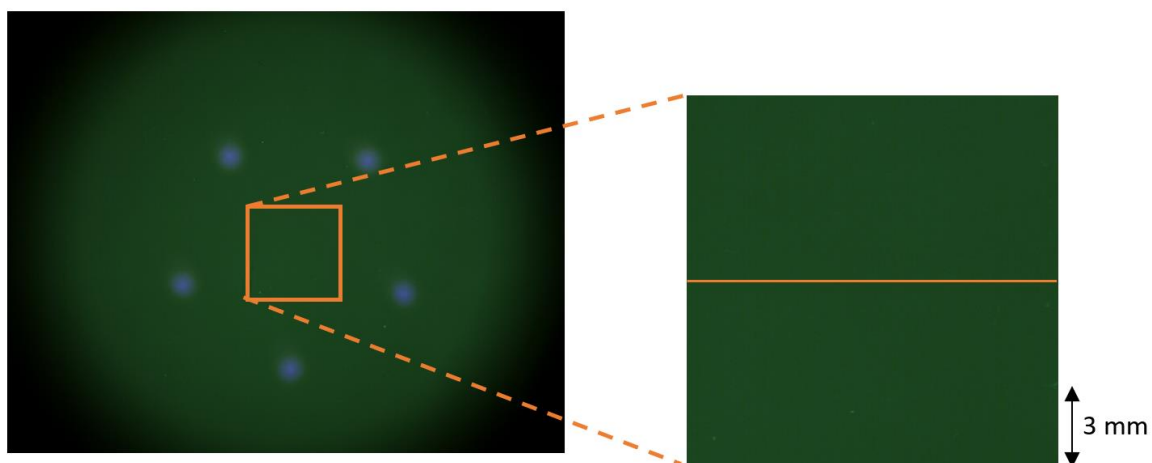


**Figure 4.1** Intensity measured position of fluorescence image
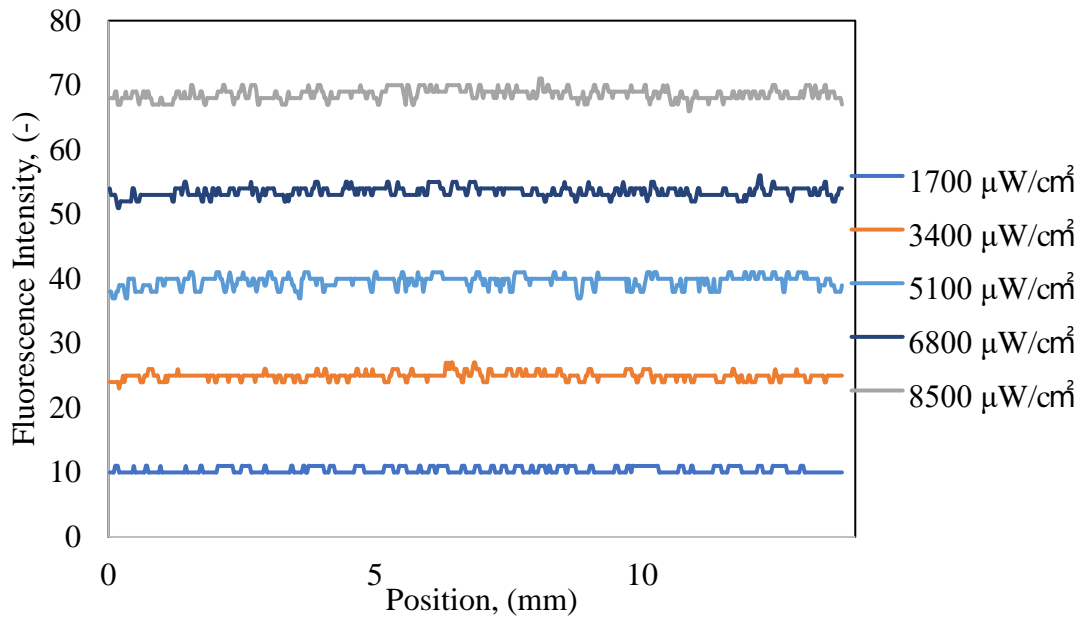
**Figure 4.2** plot profile of measured fluorescence intensity for several different U.V. light source intensity
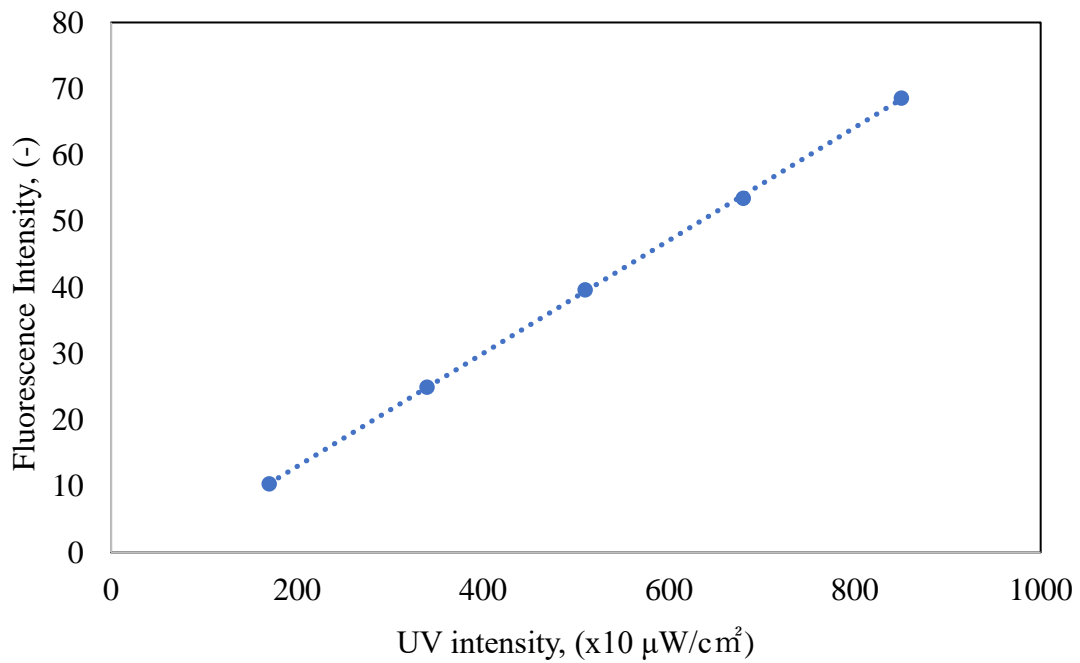


**Figure 4.3** The relationship of fluorescence intensity due to U.V. light source intensity of 25 mg/L pyranine solution

**4.1.2** The effect U.V. light source continues illumination on fluorescence intensity

The following graphs describes the fluctuation of fluorescence intensity caused by continues excitation of U.V. light source. *Figure 4.4* is the measured plot profile of fluorescence images for the first three hours of U.V. light continues illumination. The data was taken on pyranine solution 50 mg/L which was illuminated by 3400 µM/cm$^2$ U.V. light source intensity. The result shows that fluorescence intensity reduces as the continues illuminated time elapses. There are some possibilities factors affect this phenomenon. One of the possibility reasons for fluorescence intensity to reduce on continues U.V. light source continues illumination is the reduction of pyranine solution due to evaporation. *Figure 4.5* shows mass reduction of pyranine solution as time elapsed due to evaporation. The measurement was conducted under 23 °C room temperature and 65% humidity conditions, respectively. The result shows that pyranine solution reduced along with passing time. It reduced about 4% in three hours, this also means that the solution thickness decreased comparable to the same amount of evaporated water since the camber base area remain constant.
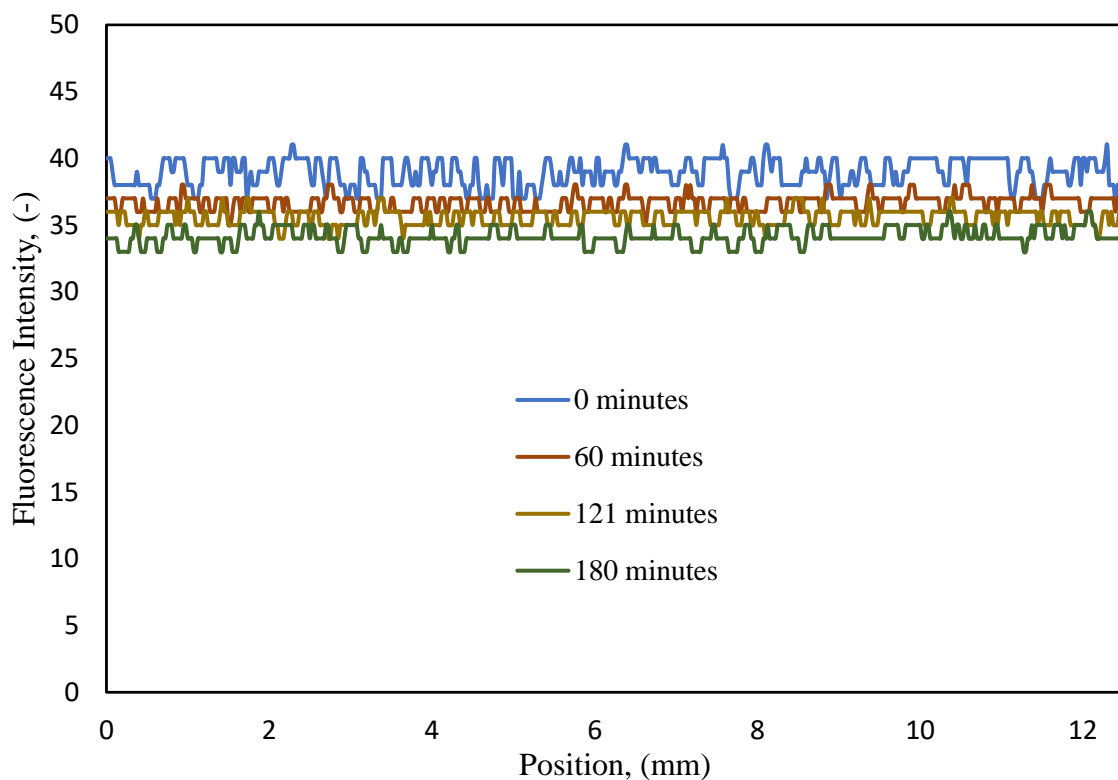


**Figure 4.4** Plot profile of fluorescence intensity due to continues illumination of U.V. light source
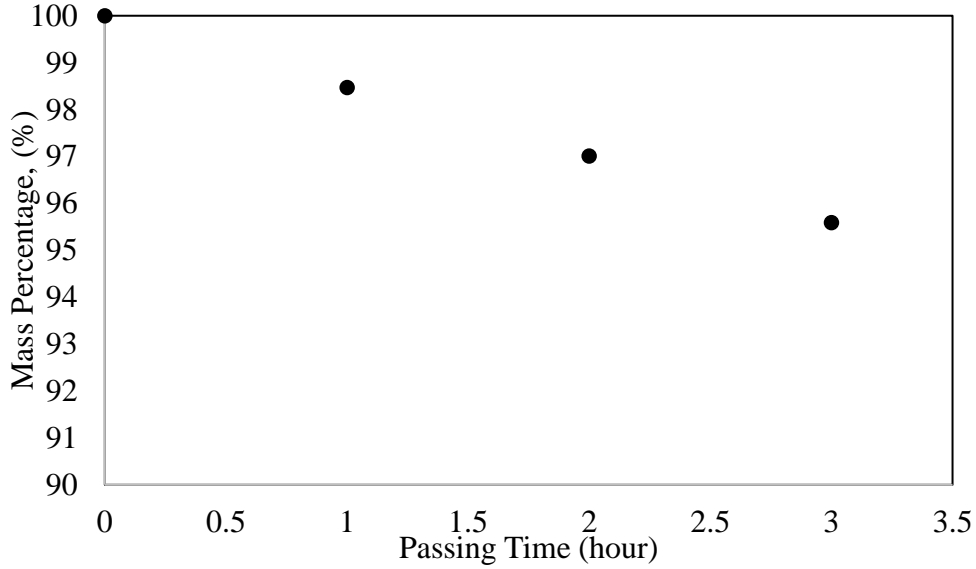
**Figure 4.5** The reduction of pyranine solution mass due to time elapsed

However, according to Beer-Lambert law the reduction of pyranine solution mass due to evaporation theoretically does not affect fluorescence intensity, because the reduction of pyranine solution mass due to evaporation increases the solution density at the same time. The explanation with Beer-Lambert law formula is shown as follows.

The concentration of dye solution is expressed as,

$$c = \frac{m_p}{V} \qquad 4.1$$

Where, $m_p$ is mass of pyranine substance within the solution and V is the volume of distillated water within the solution. After pyranine solution situated in the room temperature for several times, some water inside pyranine solution evaporated. Due to the evaporation, the solution thickness also reduces at the same ratio of evaporated water since the camber base area was same. Then the concentration after evaporation can be described as,

$$c_t = \frac{m_p}{V_t} = \frac{m_p}{A \cdot l_t} \qquad 4.2$$

$l_t$ is the remaining thickness after evaporation. So, it also can be expressed as follow,

$$c_t = \frac{m_p}{A \cdot x \cdot l} = \frac{c}{x} \qquad 4.3$$

x is the reduction ratio of solution thickness.

Then, the absorbance of pyranine solution due to evaporation is shown as,

$$A_t = \varepsilon \cdot c_t \cdot l_t \qquad 4.4$$

40

$$A_t = \varepsilon \cdot \frac{c}{x} \cdot x \cdot l \qquad\qquad 4.5$$

$$A_t = A \qquad\qquad 4.6$$

The absorbance of pyranine solution before and after evaporation was same. Therefore, theoretically the reduction of dye solution due to evaporation does not affect the transmitted fluorescence intensity, and thus intensity remain same at any given passing time.

As a confirmation, an experiment was conducted with different method, that is by covering the U.V. light source, so that there was no direct contact between U.V. light source and pyranine solution. Pyranine solution was only illuminated by U.V. light at the time of capturing the fluorescence contact image. This way additional heat from UV light source can be avoided. The result is shown in *Figure 4.6*. As shown in *Figure 4.6*, there was no change in fluorescence intensity at any given passing time. This result match completely with the theory of Beer-Lambert theory. It is an evident that the evaporated fluorescence solution does not reduces captured fluorescence intensity.
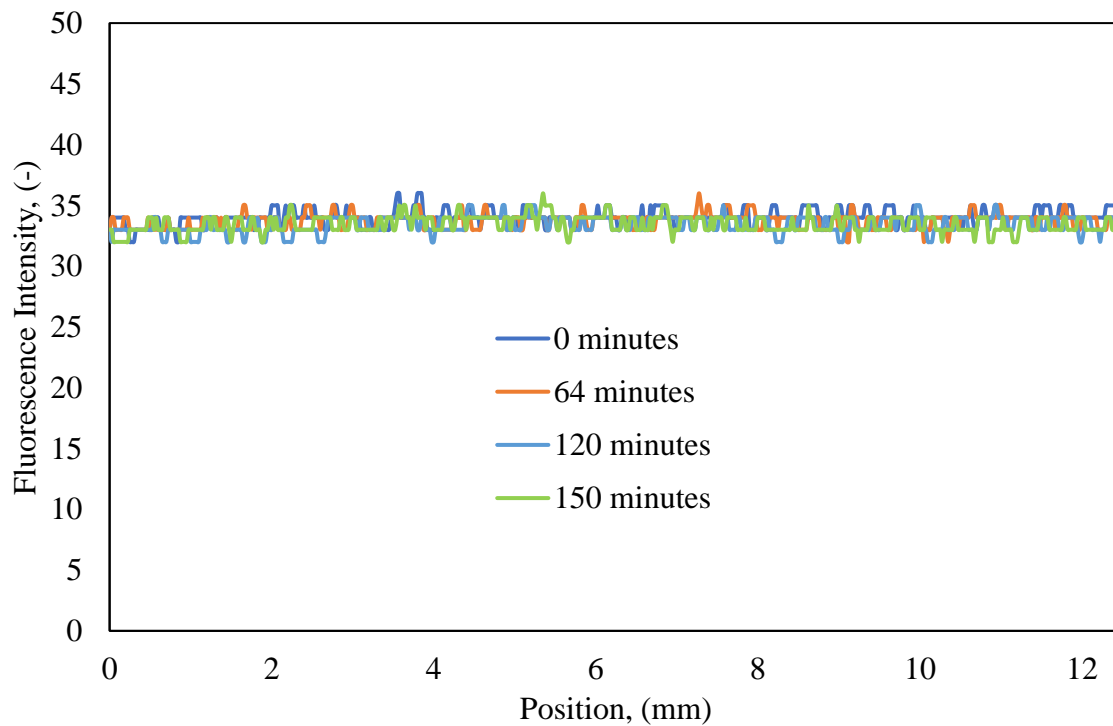


**Figure 4.6** Plot profile of fluorescence intensity due to time elapses without continues contact with U.V. light sources

Other possibility that might affect fluorescence intensity shown in *Figure 4.4* is temperature rise due to continues illumination of U.V. light source. To investigate the involving temperature on continues U.V. light illumination, the temperature fluctuation on pyranine solution was measured. *Figure 4.7* shows the fluctuation of pyranine solution temperature because of continues illumination of U.V. light source for about 5 hours. It is clear enough that the heat emitted from U.V. light source was not sufficient to increase the temperature of pyranine solution. Thus, it concluded that the reduction of fluorescence intensity on our system shown in *Figure 4.4* was not caused by temperature change.
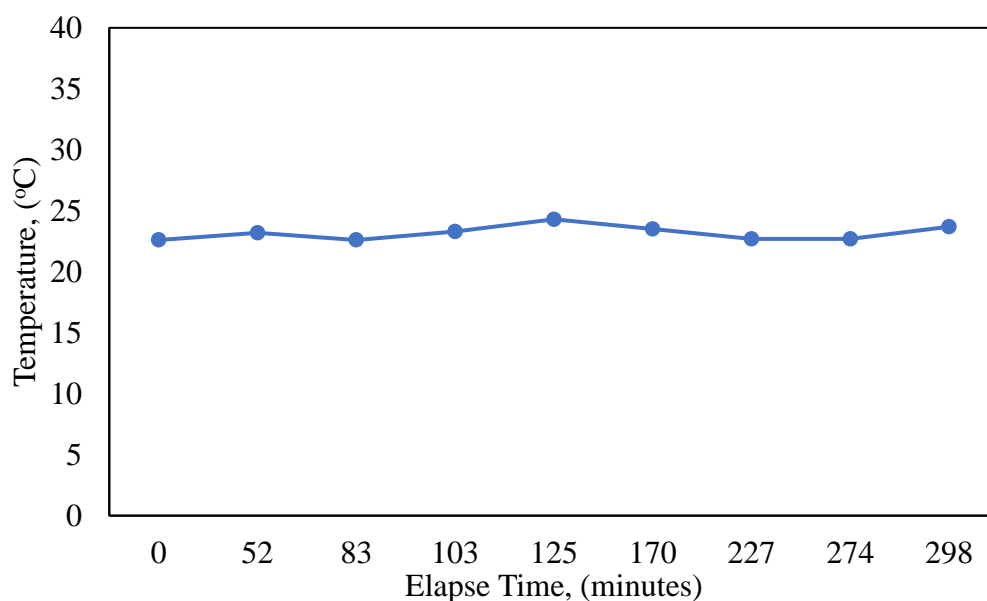


**Figure 4.7** Pyranine solution temperature fluctuation due to continues U.V. light illumination

The data shown above implied that the reduction of fluorescence intensity in our system was not caused by continues illumination of U.V. light due to its temperature rise or the effect of evaporation. However, the degradation of fluorescence light was cause by the quenching effect due to U.V. light source illumination. Accordingly, in order to avoid quenching light effect, the U.V. light need to be covered.

**4.1.3** Calibration

   The calibration of pyranine dyed fluorescence intensity was measured on multiple pyranine solution density, they are 25 mg/L, 50 mg/L, 100 mg/L, 200 mg/L, 400 mg/L, 800 mg/L, 1600 mg/L and 3200 mg/L, eight different densities, respectively. *Figure 4.8* displays the simple schematic system of calibration method. In the calibration, the rubber material was attached on the top of micrometer with accuracy 0.001 mm. It was moving down every 0.01 mm for each image captured for measurement. At lower density of pyranine solution, however, the image captured for up to 0.2 mm range based on the thickness range measurement.

   *Figure 4.9* shows the calibration result of fluorescence intensity for 3200 mg/L density of pyranine solution, while *Figure 4.10* describes fluorescence intensity calibration for all densities of pyranine solution. As shown in *Figure 4.9*, fluorescence intensity increased as solution thickness increased, and it then deteriorated at higher solution thickness. As the fluorescence intensity decays at higher solution thickness, finding the limit of linear line in fluorescence intensity curve become essential for calibration of fluorescence microscopy. The limit of linear line for 3200 mg/L density of pyranine solution in *Figure 4.9* shown at the point of 0.0163 mm of solution thickness in which the vertical line was drawn. Through this, we understood that using 3200 mg/L density of pyranine solution, our fluorescence microscopy device can be used to measure thickness up to 0.0163 mm. Over than that thickness the accuracy will be questionable.

   *Figure 4.10* shows Fluorescence intensity due to pyranine solution thickness for 8 variation of pyranine solution densities. The graph describes the intensity of fluorescence due to solution thickness, where the higher pyranine solution used the higher intensity of fluorescence was obtained at the same thickness. However, the range of linear line measurement was wider/thicker at low level pyranine solution densities. Therefore, low-level solution densities are often used for wide range measurement, while the high-level solution densities are usually used at thin range of measurement. Moreover, the graph also shows that the maximum intensity of solution 200 mg/L density and over were same at around 180. And the rest of densities of solution would also reach the maximum value at around the same intensity as long as the measurement conducted at enough gab for the maximum intensity to reach.

   Lastly, *Figure 4.11* was arranged to display the measurement thickness linear of limit for each provided pyranine solution density. As shown in *Figure 4.11*, the maximum thickness of linear of line (LOL) decreased significantly as the pyranine solution density increased up to

200 mg/L, and then it reduced slightly afterward. This information should benefit researcher in finding proper pyranine solution density based on the measurement of thickness range.
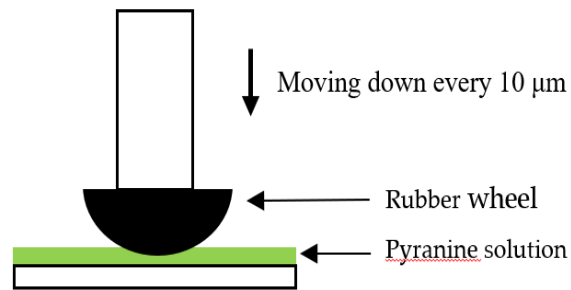


**Figure 4.8** Configuration system of calibration
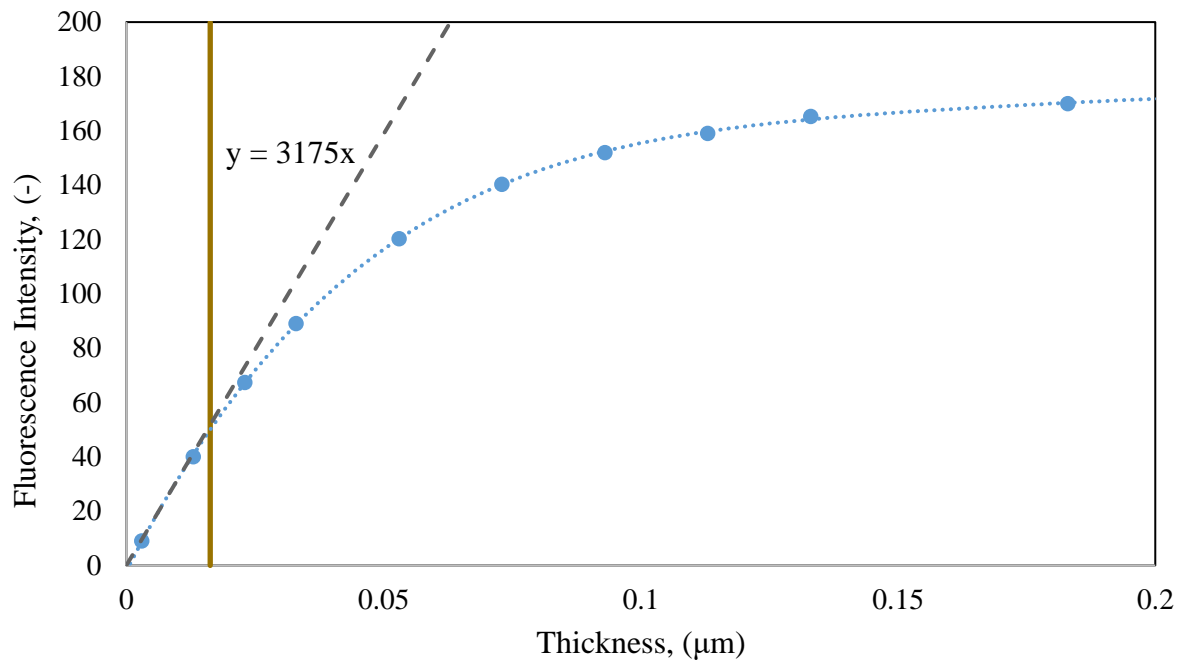


**Figure 4.9** Fluorescence intensity calibration using 3200 mg/L density of pyranine solution
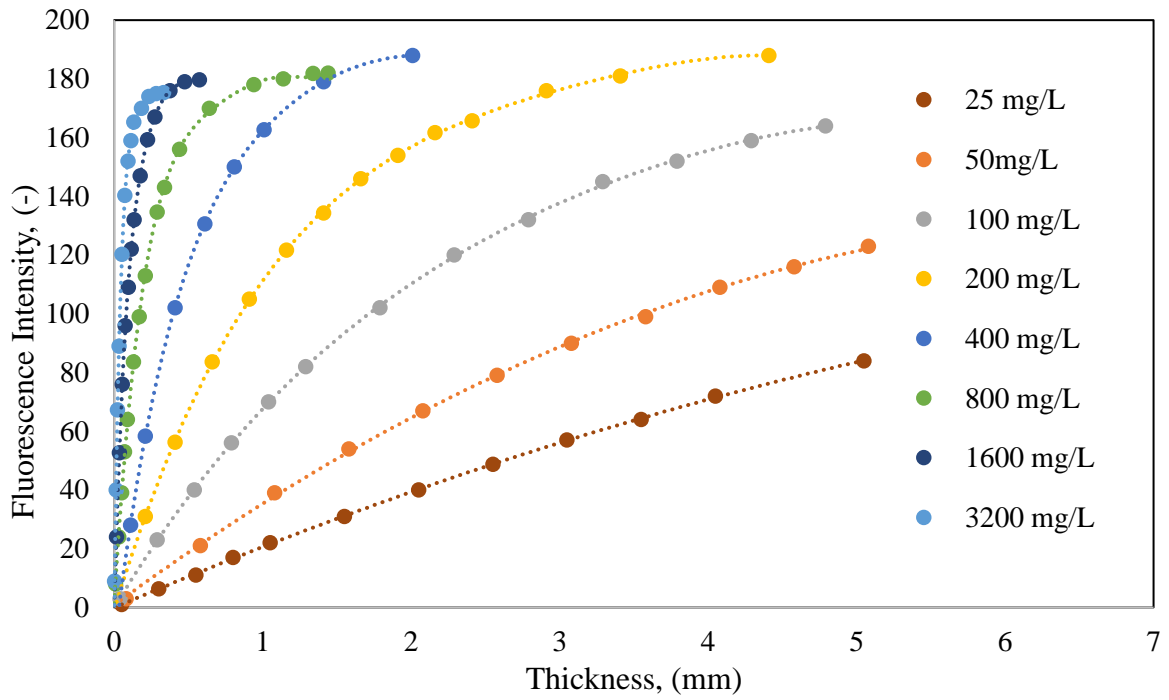
**Figure 4.10** Pyranine dyed fluorescence intensity calibration for several solution densities



$y = 50x^{-1}$
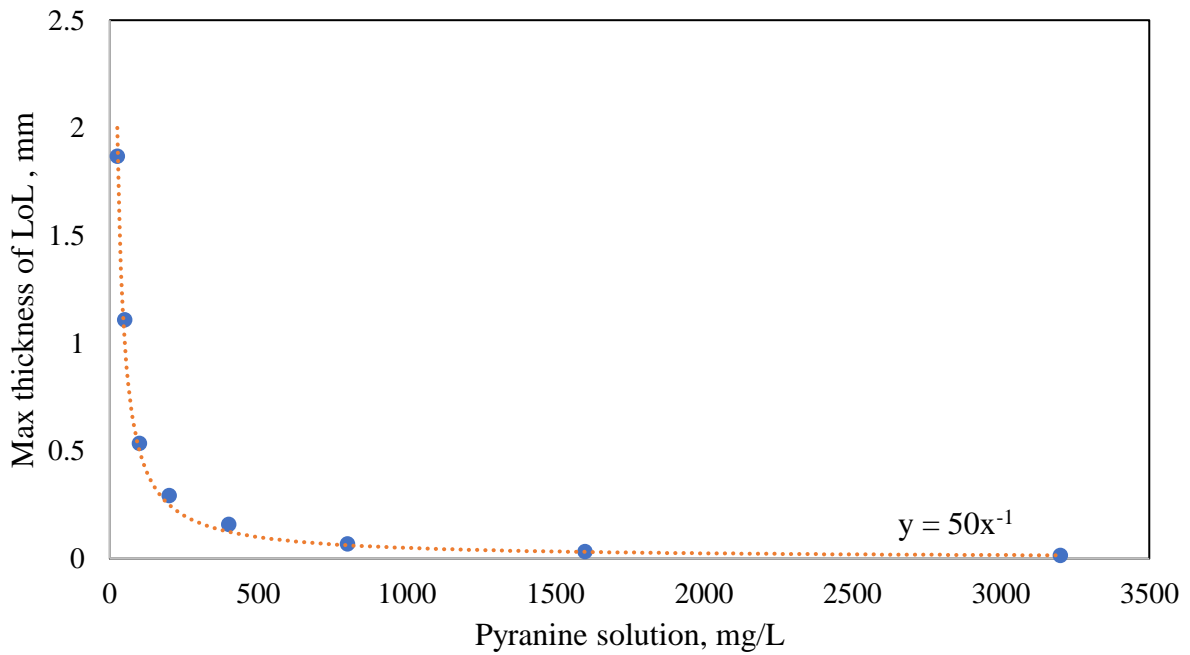
**Figure 4.11** Maximum thickness of linear of line on fluorescence calibration for several densities of pyranine solution

## 4.2 Rubber-wheel contact on flat surface

### 4.2.1 Static rubber contact

As rubber-wheel is in touch with flat surface of glass plate, the main cause of frictional is adhesion force. At the same time, the applied load on rubber-wheel wider the contact area due to its viscoelasticity. *Figure 4.12* and *Figure 4.13* show the binary images of the apparent and the real contact area between rubber-wheel and flat surface of glass plate for several selected applied loads in static test. In general, the binary images of the real contact area were smaller than the apparent contact area. There are some parts within the real contact area were not in contact between rubber-wheel and flat surface indicating the rubber-wheel was not perfectly smooth. Also, there was non-contact region on the right side of rubber-wheel contact. All of these non-contact parts can only be confirmed with real contact area binary image. The experiment for static contact was carried out three times, the detail information about the apparent and the real contact area are shown in *Table 4.1* and *Table 4.2*.

As shown in *Figure 4.12* and *Figure 4.13*, both apparent and real contact areas between rubber-wheel and flat surface was wider as the applied normal load increased. This development indicating load influence on rubber-wheel contact area. The higher load applied on rubber-wheel the more it deformed and then forming wider contact area. Previously, we had reported load dependency of rubber-wheel contact area in a conference [50]. However, we could not identify the increasing pattern of contact area because the number of data was very small. Therefore, in the current study we conducted experiment with enough variation of applied normal loads to obtain more precise information. *Figure 4.14* and *Figure 4.15* show the graph of plotted contact area of rubber-wheel for both apparent and real contacts. The plotted contact area of rubber-wheel for every applied normal load from three times trials were distributed within the range about 20 mm$^2$ on each applied load. Also, the contact area of rubber-wheel increased as applied normal load increased. However, the effect of applied normal load on rubber-wheel contact area was deteriorated at higher applied loads forming logarithmic pattern of trendline from start to the end. This phenomenon implying the resistance of rubber-wheel at higher applied load was also higher. It makes the increment of contact area of rubber-wheel at higher load become smaller.

**Figure 4.12** Fluorescence images of rubber-wheel apparent contact due to applied normal loads (images belong to trial 2)
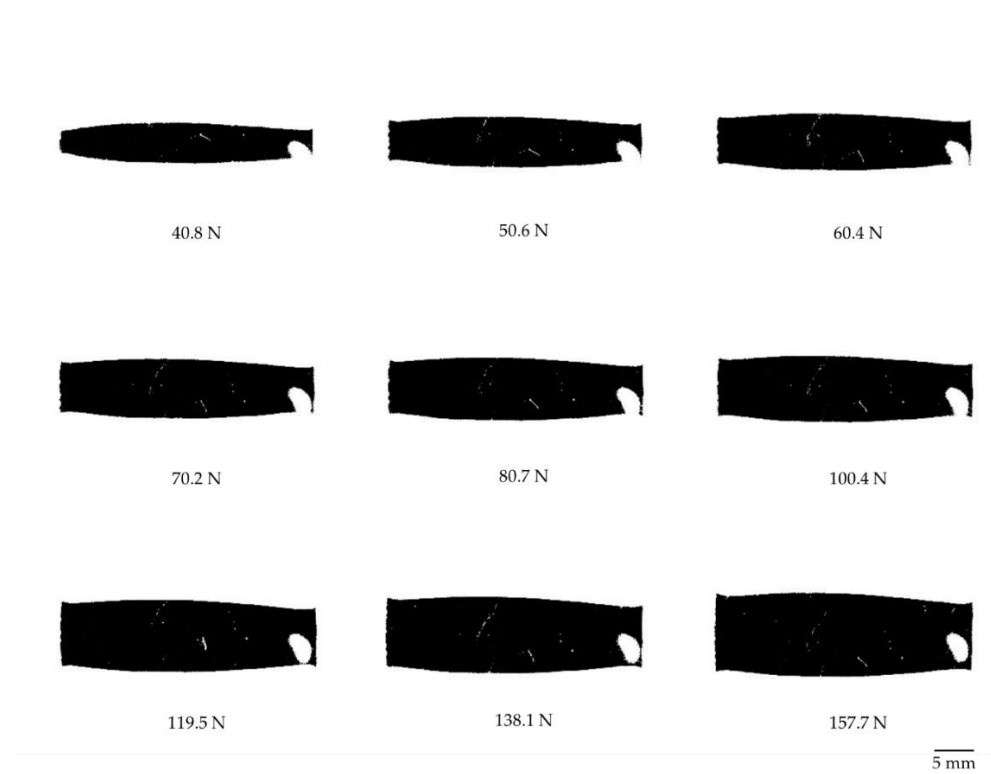


**Figure 4.13** Fluorescence images of rubber-wheel real contact due to applied normal loads (images belong to trial 2)

**Table 4.1** The measured apparent contact area of rubber-wheel due to applied load

| Load (N) | Apparent contact area (mm$^2$) | | |
|---|---|---|---|
| | Trial 1 | Trial 2 | Trial 3 |
| 40.8 | 168.7 | 163.8 | 158.9 |
| 50.6 | 200.4 | 201.4 | 179.7 |
| 60.4 | 207.6 | 223.1 | 206.0 |
| 70.2 | 226.1 | 233.7 | 244.4 |
| 80.7 | 244.7 | 245.6 | 240.5 |
| 90.5 | 257.1 | 257.0 | - |
| 100.4 | 286.0 | 280.1 | - |
| 119.5 | 312.2 | 295.8 | 293.3 |
| 138.1 | 334.9 | 323.1 | 313.5 |
| 157.7 | 356.7 | 350.9 | 327.2 |

**Table 4.2** The measured real contact area of rubber-wheel due to applied load

| Load (N) | Real contact area (mm2) | | | |
|---|---|---|---|---|
| | Trial 1 | Trial 2 | Trial 3 | Average |
| 40.8 | 126.7 | 124.0 | 116.9 | 122.5 |
| 50.6 | 159.8 | 162.0 | 138.5 | 153.4 |
| 60.4 | 167.0 | 184.3 | 165.6 | 172.3 |
| 70.2 | 186.0 | 195.4 | 204.6 | 195.3 |
| 80.7 | 204.2 | 207.3 | 200.8 | 204.1 |
| 90.5 | 217.5 | 219.0 | 204.1 | 213.5 |
| 100.4 | 247.3 | 242.3 | 214.3 | 234.6 |
| 119.5 | 274.7 | 258.2 | 255.4 | 262.8 |
| 138.1 | 297.5 | 286.5 | 276.9 | 287.0 |
| 157.7 | 320.2 | 314.5 | 289.0 | 307.9 |
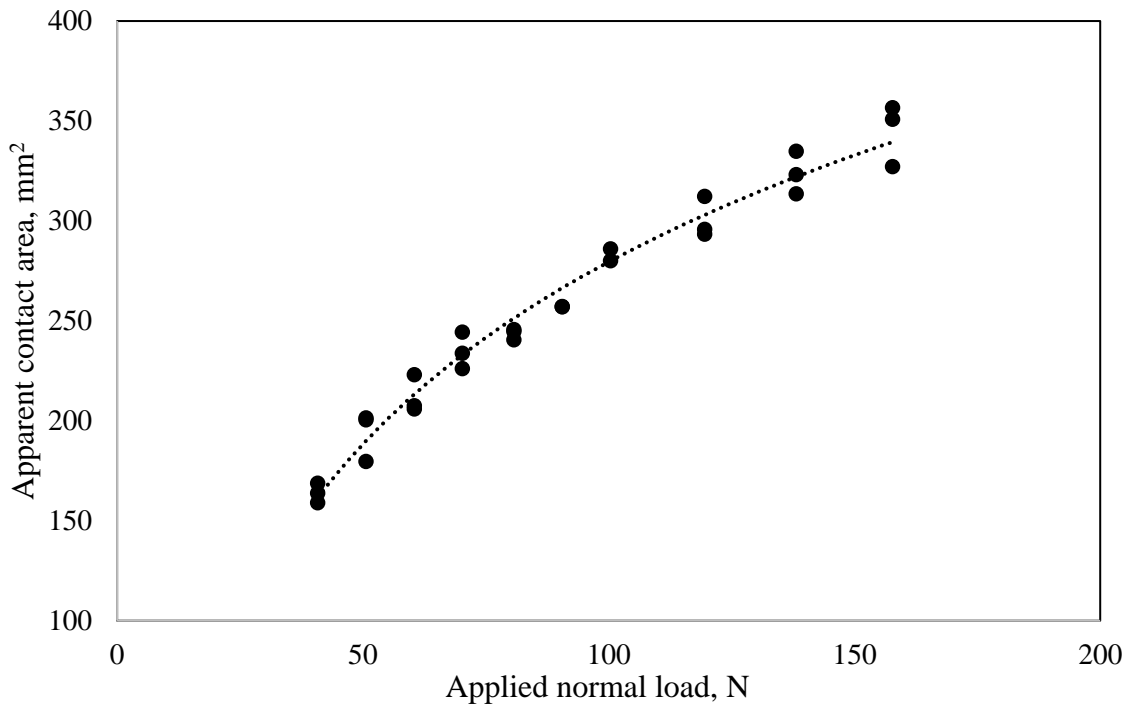
**Figure 4.14** Relationship between rubber-wheel apparent contact area and applied normal load for static condition
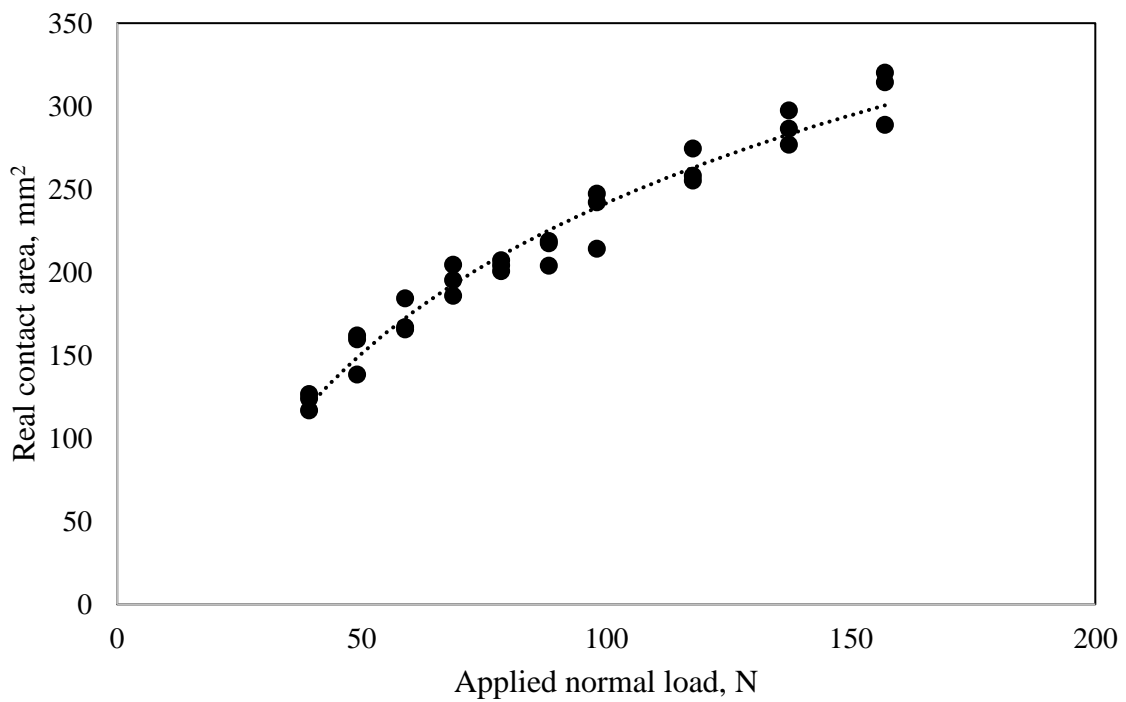


**Figure 4.15** Relationship between rubber-wheel real contact area and applied normal load of static condition

The comparison of theoretical with experimental rubber-wheel contact area is shown in *Figure 4.16*. The experimental data procured based on determination method of Otsu thresholding technique explained in section 3.4. The theoretical data was obtained through calculation process using Hertz theory for cylindrical solid model as shown in equation *2.17*. As displayed in *Figure 4.16*, the apparent and the real contact areas between rubber-wheel and flat surface were increased as the applied normal load increased in similar tendency. The apparent contact area for each applied normal load were wider about 40 mm$^2$ compared to the real contact area. Other information can be obtained from the graph is that the experimental data of the real contact area match well with theoretical data at higher applied normal load. In contrast with the real contact area, the apparent contact area of rubber-wheel on flat surface has smaller gap with theoretical data at lower applied normal load and wider at higher applied normal load.
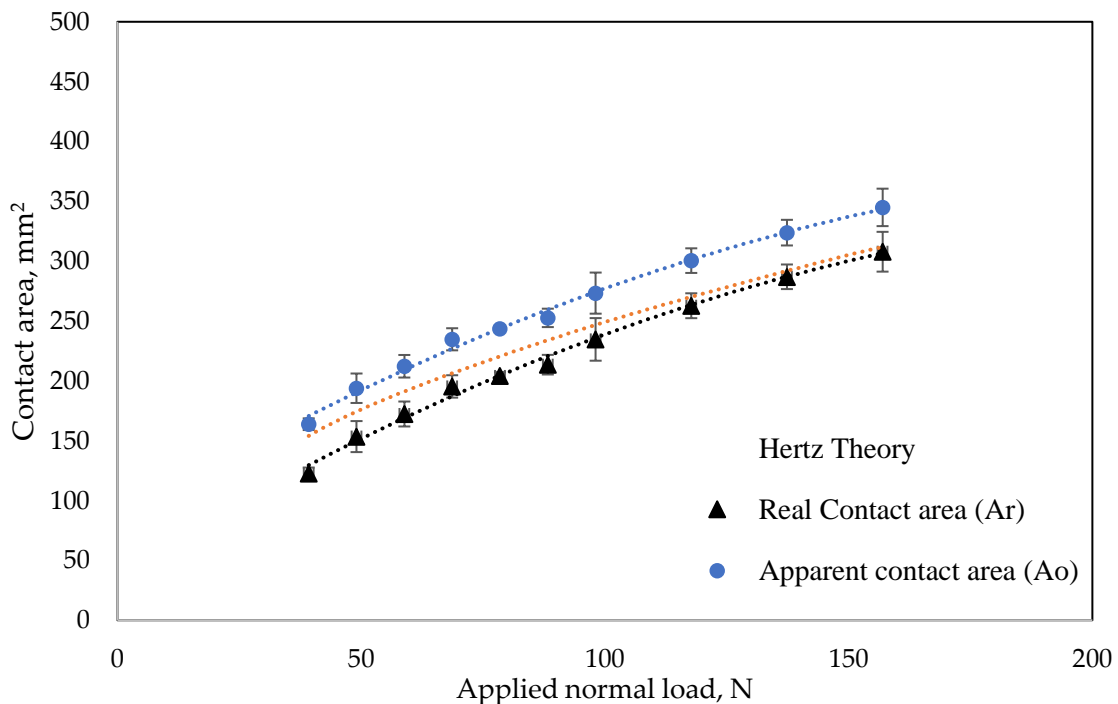


**Figure 4.16** Rubber-wheel contact comparison between theoretical and experimental contact area

*Figure 4.17* illustrates the ratio of real and apparent contact area between rubber-wheel and flat surface. The graph describes the ratio of real and apparent contact area as it increased slightly due to applied normal load. This information indicating the effect of static applied normal load on rubber-wheel real contact area was slightly bigger than that on the apparent contact area.
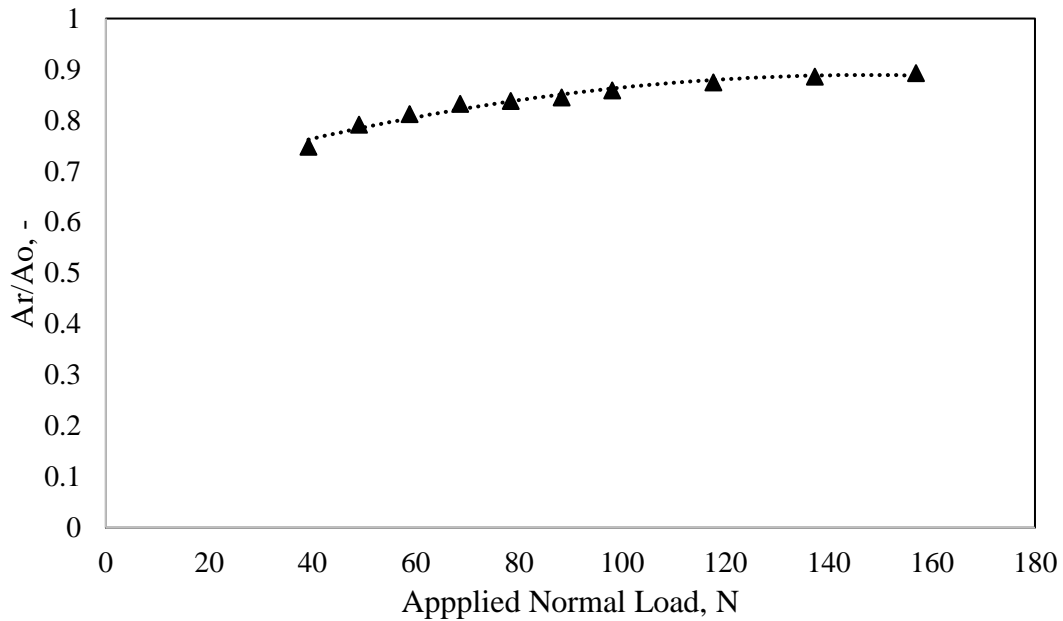
**Figure 4.17** Real and apparent contact ratio of rubber-wheel on flat surface

**4.2.2** Dynamic rubber contact

The contact area images show in *Figure 4.18* and *Figure 4.19* illustrate the contact condition of apparent and real contacts between a rubber-wheel and flat surface when a loaded rubber-wheel moving at six (out of seven) selected moving speed of 2, 8, 20, 40, 80, and 160 mm/s, respectively. The high speed camera recorded moving images along the path using 100 fps and 1/200 shatter speeds. The actual amount of measured apparent contact area and real contact area of rubber-wheel due to seven variant moving speeds area shown in *Table 4.3* and *Table 4.4*.

As can be seen in *Figure 4.18*, there is something that popped out from the rubber-wheel contact area in form of pillars which was oxygen. The oxygen bubbles sometimes formed within pyranine solution of stuck on flat glass of stuck on the surface of rubber-wheel that could not be seen from outside. When the rubber-wheel moving on flat surface, the oxygen pushed on forward and forming pillars pattern, some of theme longer and thick, and some others smaller. *Figure 4.20* shows how the oxygen pillars formed during rubber-wheel movement. At the start there were two visible oxygen stacked on flat surface of glass and some oxygen bubbles can be seen within pyranine solution. Then, as rubber-wheel moving closer to the oxygen, the oxygen bubbles stretched to the rubber-wheel. Lastly, the oxygen pillar was formed and moving along with rubber-wheel.
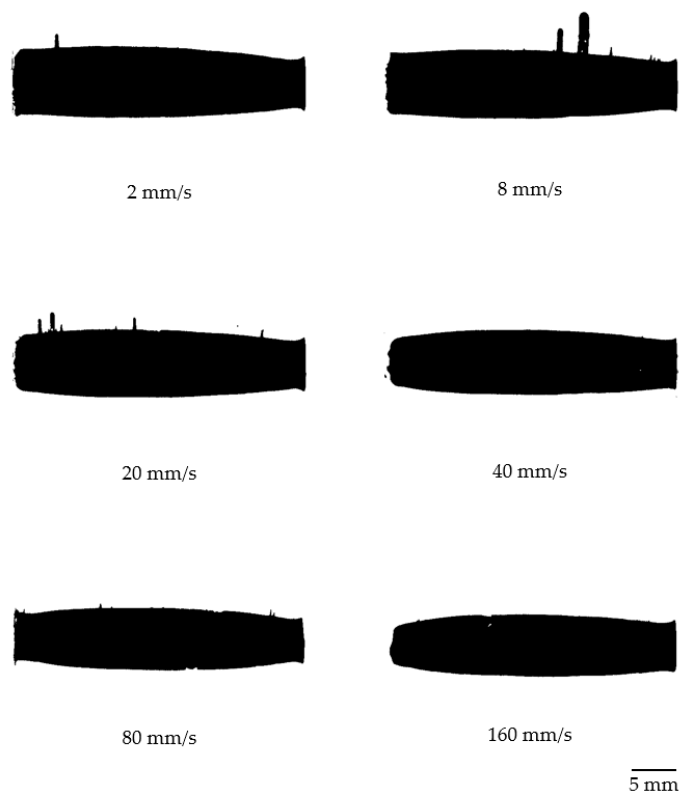
**Figure 4.18** Images of the apparent contact area for six different moving-speeds at the same contact position (images belong to applied load 80.7 N)

2 mm/s

8 mm/s

20 mm/s

40 mm/s

80 mm/s

160 mm/s

5 mm
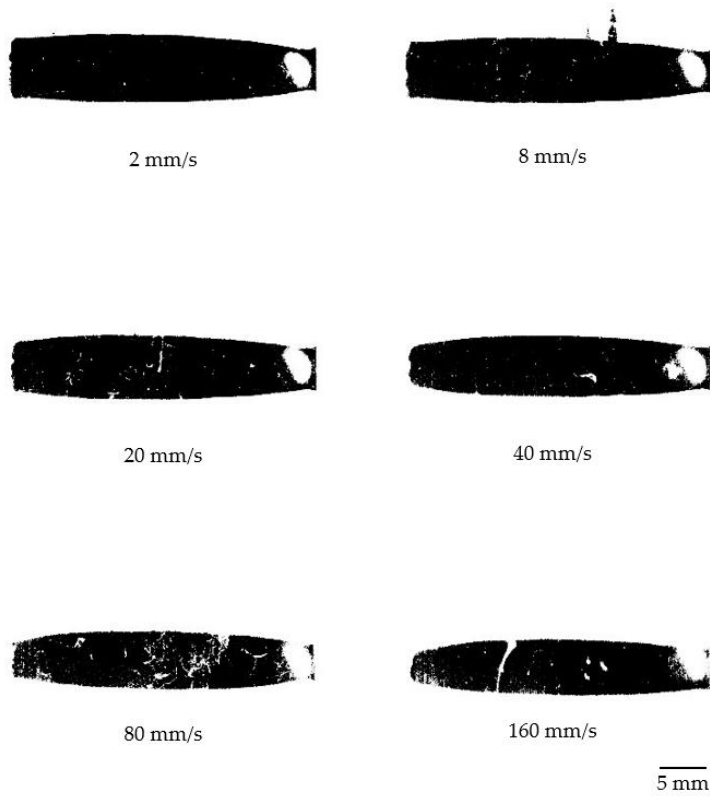


**Figure 4.19** Images of the real contact area of six different moving-speeds at the same contact position (images belong to applied load 80.7 N)

2 mm/s

8 mm/s

20 mm/s

40 mm/s

80 mm/s

160 mm/s

5 mm

52

**Table 4.3** The measured apparent contact area of rubber-wheel due to moving speeds

| Speed (mm/s) | Apparent contact area (mm$^2$) | | | | |
|---|---|---|---|---|---|
| | Load 40.2 N | Load 60.8 N | Load 80.4 N | Load 99.0 N | Load 121.5 N |
| 2 | 154.47 | 183.80 | 220.29 | 230.57 | 256.36 |
| 4 | 159.43 | 176.69 | 209.18 | 231.22 | 253.32 |
| 8 | 168.10 | 187.37 | 212.13 | 237.16 | 255.42 |
| 20 | 165.38 | 180.97 | 208.28 | 228.64 | 249.94 |
| 40 | 155.26 | 172.11 | 196.84 | 219.85 | 247.84 |
| 80 | 148.85 | 164.13 | 189.06 | 208.69 | 245.80 |
| 160 | 138.08 | 163.58 | 184.82 | 217.10 | 241.17 |

**Table 4.4** The measured real contact area of rubber-wheel as the effect of moving speeds

| Speed (mm/s) | Real contact area (mm$^2$) | | | | |
|---|---|---|---|---|---|
| | Load 40.2 N | Load 60.8 N | Load 80.4 N | Load 99.0 N | Load 121.5 N |
| 2 | 112.77 | 144.70 | 182.47 | 190.56 | 219.80 |
| 4 | 117.67 | 137.37 | 170.60 | 194.10 | 216.42 |
| 8 | 126.37 | 146.25 | 172.87 | 200.25 | 217.21 |
| 20 | 123.11 | 138.46 | 166.37 | 190.09 | 212.13 |
| 40 | 110.58 | 126.47 | 152.27 | 178.64 | 207.37 |
| 80 | 100.46 | 100.36 | 131.59 | 163.17 | 204.17 |
| 160 | 82.30 | 111.10 | 129.60 | 159.43 | 191.98 |
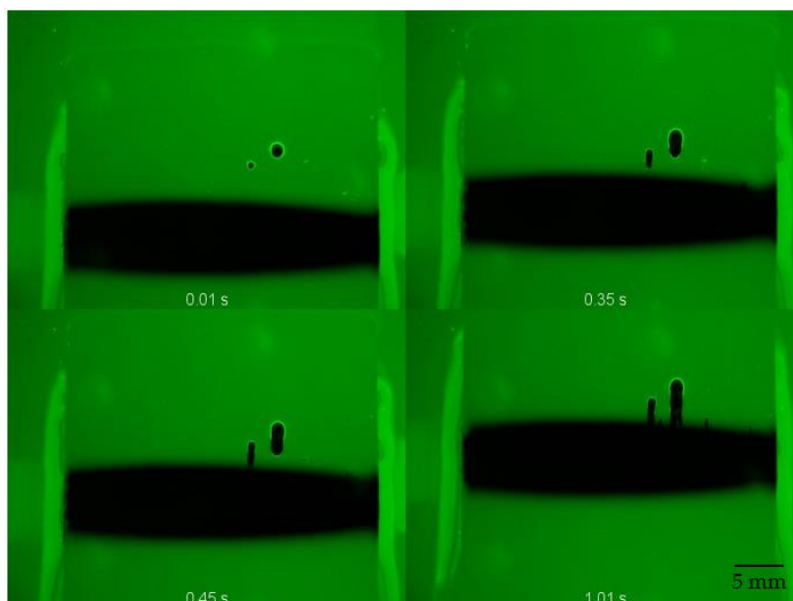


**Figure 4.20** The formation of oxygen pillars on rubber-wheel contact image (images belong to 8 mm/s moving speed under 80.4 N applied load)

*Figure 4.21* and *Figure 4.22* display the graph of rubber-wheel apparent contact area and real contact area as the influence of seven selected moving speeds. Each graph displays five different lines of rubber-wheel contact area showing five applied normal loads on dynamic (moving) test. In general, the apparent contact area and real contact area of rubber-wheel both fluctuated in similar pattern of trendline as it increased reaching the peak at around 8 mm/s, and then decreased afterwards. Both graphs also describe the effect of applied load on moving rubber-wheel, as it increased along with applied loads. The other information can be procured from the graph is that the influence of moving speed at higher applied load was less than that at lower applied normal load. It can be seen as the contact area fluctuation at higher applied load less intense compared to the lower applied normal load. The only different between the apparent contact area and the real contact area is that the measured real contact area was around 40 mm$^2$ smaller than that of apparent contact area.

As reported by Michelin [5], due to the influence of stress frequency, rubber material is divided into three states. They are rubbery state that occurs at low frequency, and then as the frequency increases the rubber material appears to be visco-elastic which is the most ideal condition for grip performance. Lastly, it becomes glassy state as the frequency increases further. The adhesion bond between rubber-wheel and flat surface of glass plate is formed and separated repeatedly as rubber-wheel moving along the path. Based on these conditions, at lower speed where the stress frequency of rubber is low, the contact area of rubber-wheel increased as moving speed increased because the rubbery state of rubber could easily deform. The possible reason for the contact area to increase at lower speed is likely due to similar phenomenon as junction growth theory. When the rubber-wheel moving at low speed, rubber-wheel was in the condition of rubbery state. Due to the influence of adhesion force, the separation speed between rubber-wheel and flat surface was lower than that of formation speed, making it look like the junction between rubber-wheel and flat surface growth. As a result, the contact area increased as moving speed increased at moving speed less than 8 mm/s. However, as the moving speed increased more than 8 mm/s the viscous characteristic of rubber became dominant leading to a glassy state. Therefore, the contact area of rubber-wheel decreased as moving speed increased. Similar phenomena also reported by Manfred Kluppel et.al. when they reported the relationship of coefficient of friction and speed at lower speed [51].

**Figure 4.21** Rubber-wheel apparent contact area on dynamic condition with five variant applied loads; 40.2 N, 60.8 N, 80.4 N, 99 N and 121.5 N, respectively.



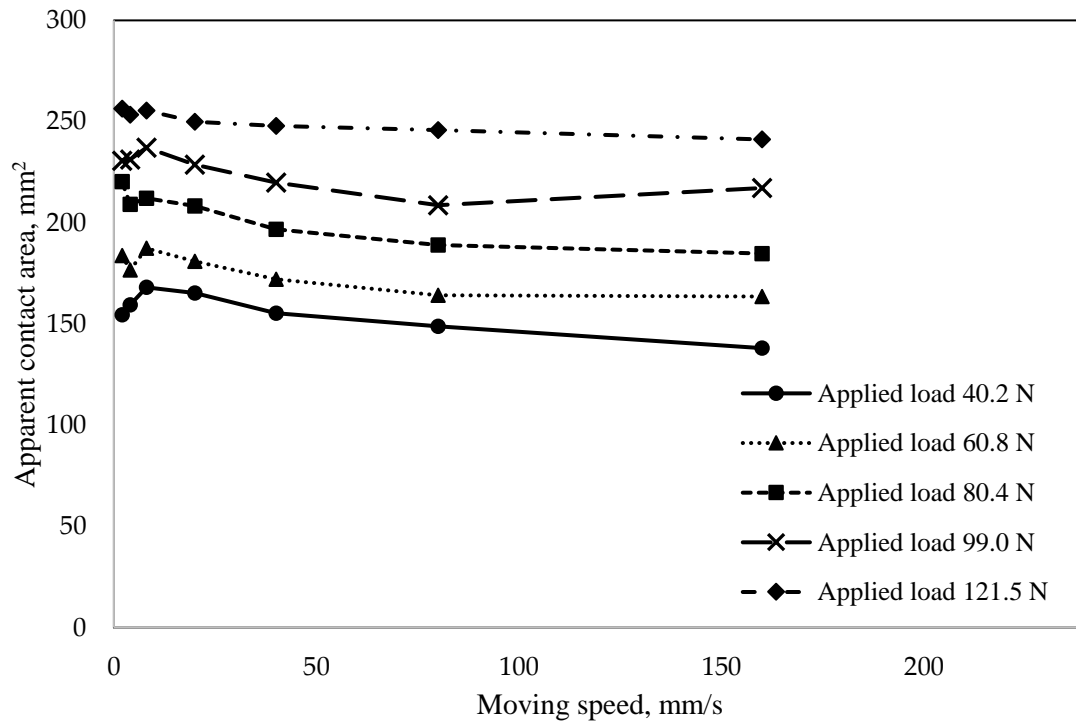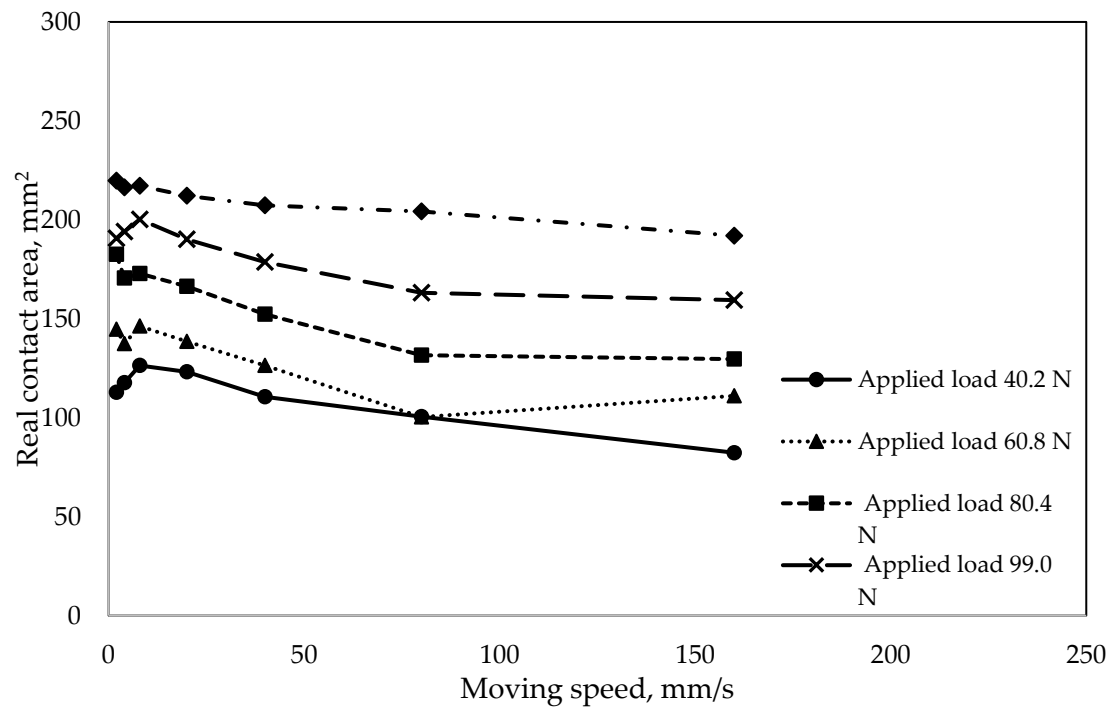**Figure 4.22** Rubber-wheel real contact area on dynamic condition with five variant applied loads; 40.2 N, 60.8 N, 80.4 N, 99 N and 121.5 N, respectively.

## 4.3 Rubber contact with road replica

### 4.3.1 Static rubber contact

It was reported that the generation of tire rubber grip (coefficient of friction) is caused by indentation and molecular adhesion stress mechanisms, respectively. Since rubber-wheel is viscoelastic, it deforms and adapts to the road surface texture when the normal load is applied. Moreover, a contact area is formed through the molecular interaction between rubber-wheel surface and road surface, generating a coefficient of friction. *Figure 4.23* shows the red color binary image of the contact area between the cylindrical rubber-wheel and road surface replica. This represents eight selected applied normal loads of static condition test and the measured rubber-wheel apparent contact area in form of graph is shown in *Figure 4.24*. The red color binary is presented in *Figure 4.23* as to make it easy to detect which part of the road surface were in contact with the rubber-wheel. It was easy to distinguish between contact and non-contact regions due to significant color differences. The red color representing the apparent contact area, while others indicating the non-contact area. However, it was quite challenging to measure the actual amount of the apparent contact area based on the image colors only. Therefore, the Otsu thresholding method was needed to obtain the proper thresholding boundary for measuring the apparent contact area of the images. As previously explained in section 3.4, the thresholding value obtained for the apparent contact area was 36. Consequently, the intensity 36 and below was considered as apparent contact region, and the intensity above 36 was regarded as a non-contact region.

*Figure 4.24* shows the relationship between the apparent contact area of rubber-wheel and applied normal load. The apparent contact area was larger as the applied normal load increased. This means that the higher normal load applied on the system, the larger rubber-wheel deformed. Additionally, as the rubber-wheel adapts more to the texture of the road surface, forming a larger apparent contact area. As presented in *Figure 4.24*, the apparent contact area increased almost linearly when the applied load increased up to around 70 N. The high resistance of rubber-wheel on higher applied load deteriorates the expansion of the apparent contact area, forming a logarithmic pattern of the trendline.
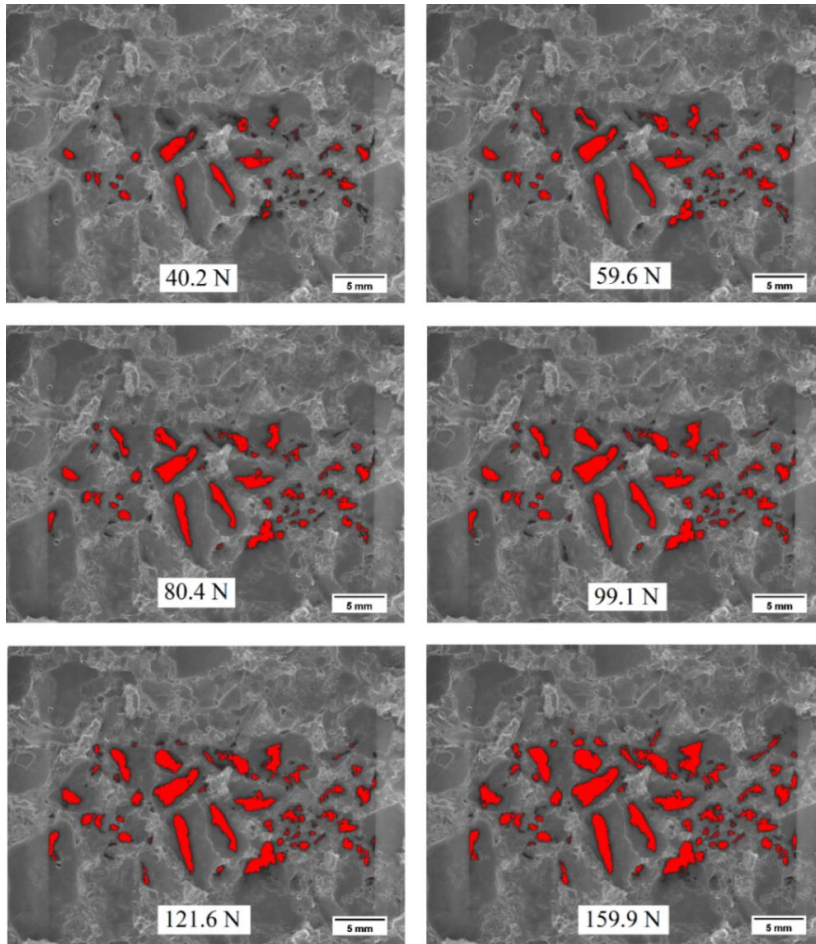
**Figure 4.23** Fluorescence images of rubber-wheel real contact on road surface due to applied normal loads
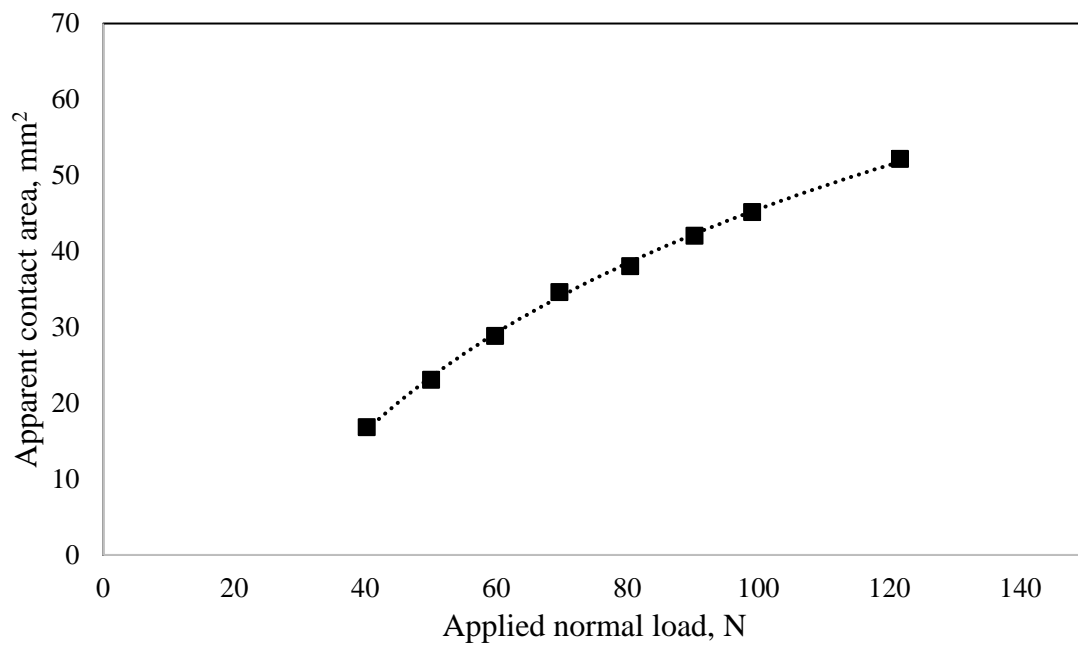


**Figure 4.24** Rubber-wheel apparent contact area due to applied load on road surface for static condition

**4.3.2** Dynamic rubber contact

The dynamic contact images shown in *Figure 4.25* illustrates the contact condition between a rubber-wheel and road surface replica when moving at 40 mm/s under an applied normal load of 40.2 N. The high speed camera recorded the moving images along the path using 100 fps. This means it took 0.75 s to cross the camera capture area of 30 mm. *Figure 4.25* only shows 9 out of 75 images. It is sufficient to show the movement of rubber-wheel contact from one side to the other side. Each position of rubber-wheel contact revealed a divergent contact footprint pattern, displaying different amounts of the apparent contact area. *Figure 4.26* illustrated the amount of apparent contact area between rubber-wheel and road surface replica for rubber contact of 0.31s – 0.63s. The nine selected contact images displayed the entire rubber-wheel apparent contact area. Due to the irregular pattern of the road surface, the apparent contact area of the rubber-wheel in these images ranged from 11 to 15 mm$^2$. It varied according to surface roughness and pattern.
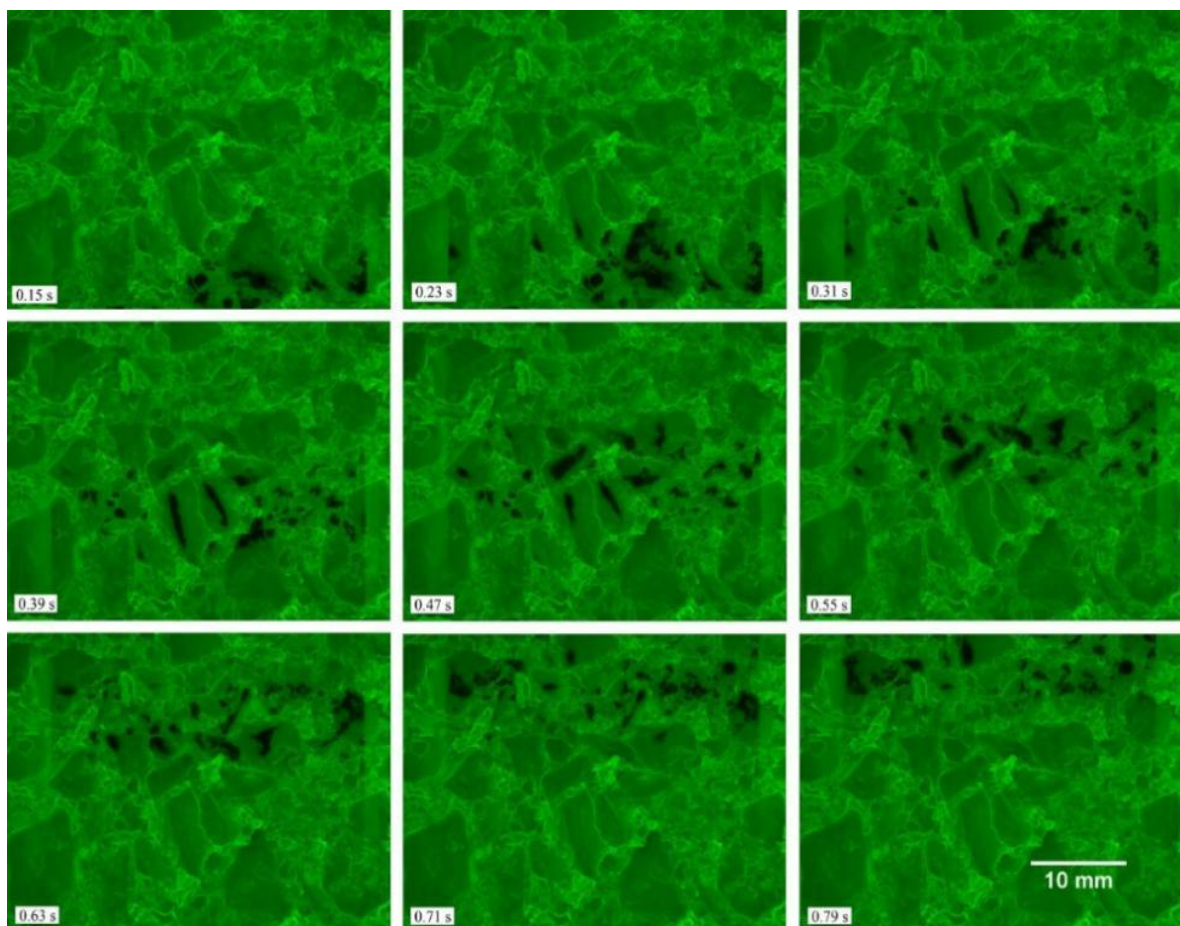


**Figure 4.25** The fluorescence images of rubber-wheel contact while running at moving speed 40 mm/s under 40.2 N of the normal load
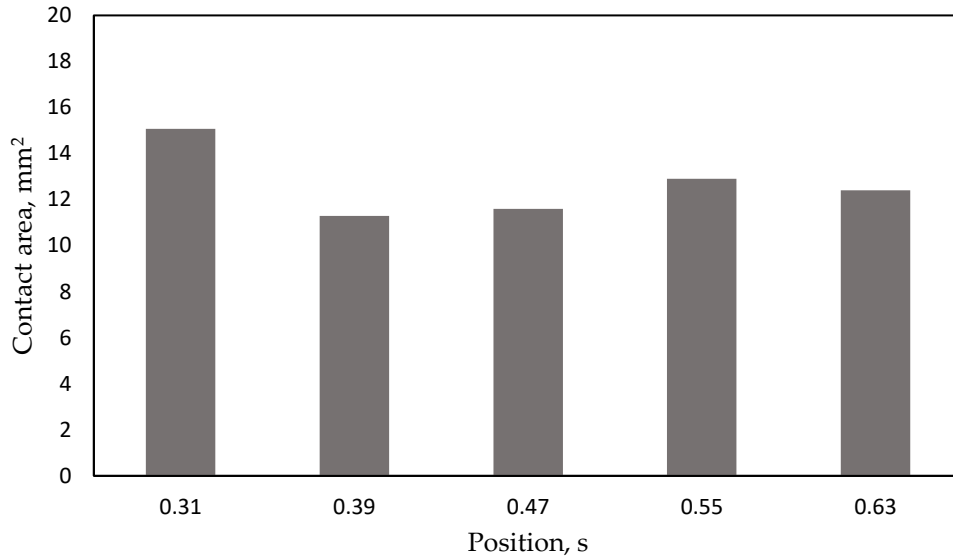
**Figure 4.26** The rubber-wheel apparent contact area of some position along track path

*Figure 4.27* shows the images of moving speed influence on the apparent contact area between a 40.2 N loaded rubber-wheel and road surface replica on the same position. The images display the apparent contact area of the rubber-wheel that decreased as the moving speed increased. The relationship between the apparent contact area of rubber-wheel and moving speed is shown in *Figure 4.28*. The grip force is produced by the molecular adhesion interaction of rubber-wheel on road surface and the indentation on the road surfaces. In adhesion friction, the bond breaks and forms repeatedly along with the rubber-wheel movement. The stretching adhesion bond gets weaker as the rubber-wheel moves at a certain high speed. Therefore, the contact area of a stationary rubber-wheel was always higher than in the dynamic condition. Additionally, due to the contact with road surface, the rough pattern of road surface increased the stress frequency of rubber-wheel making rubber-wheel state glassier. Therefore, the faster rubber-wheel moves the weakened the adhesion interaction. Similar results were reported by Binshuang Zheng and co-workers in their report titled "Adhesion Characteristic of Tire-Asphalt Pavement Interface Based on a Proposed Tire Hydroplaning Model" [19]. Consequently, the rubber-wheel apparent contact area was smaller as the moving speed increased. These phenomena were presented in all 3 type applied loads forming negative logarithmic trendline. The only different thing was that a higher applied load increased the wider apparent contact area formed. A higher applied load makes the penetration of rubber-wheel on road surface roughness deeper. Consequently, the apparent contact area of the rubber-wheel observed through fluorescence microscopy widened as the applied load increased.

There are filled marks representing the dynamic condition of the rubber-wheel contact, and unfilled marks representing static conditions shown in *Figure 4.28*. The static condition of the contact area was used as a comparison to the dynamic contact. It also helps in determining the trendline of rubber contact at a very slow moving-speed. As a result, the apparent contact area of rubber-wheel reduced considerably at moving speed below 20 mm/s. On the contrary, it reduced slightly to an almost constant line at moving speed above 20 mm/s. This shows that the apparent contact area of the rubber-wheel is highly affected by the moving speed of vehicles. Similar result was reported by Micheline, where the grip coefficient of tire reduced as vehicle speed increased [6]. Hence, there is a significant relationship between the contact area and the grip performance of the rubber tire. This can be seen when they were both decreased as the moving speed increased.
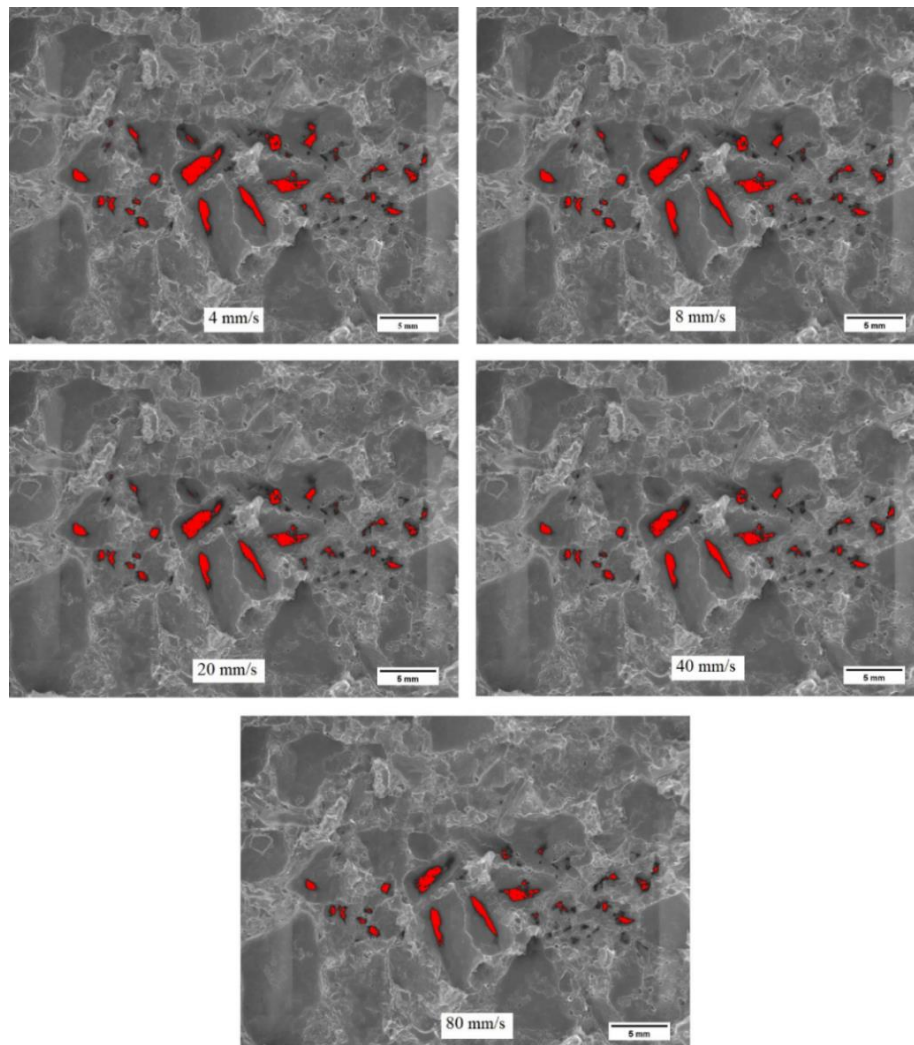


**Figure 4.27** Images of apparent contact area on road surface for five different moving speed at the same contact position (images belong to applied load 40.2 N)
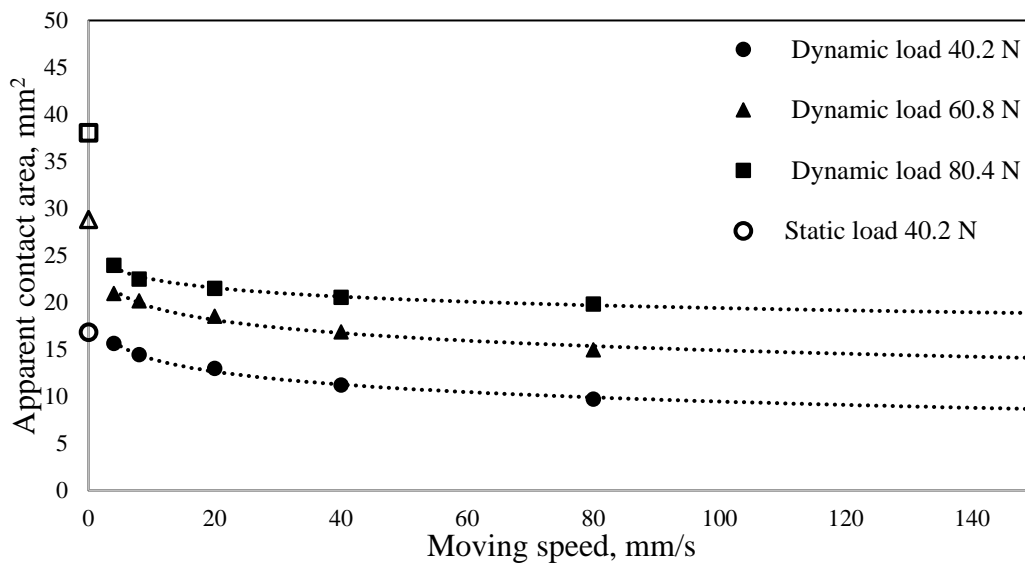
**Figure 4.28** Rubber-wheel apparent contact area with road surface on dynamic condition of three variation applied normal loads; 40.2 N, 60.8 N, and 80.4 N, respectively

## 4.4 Rubber-wheel contact area comparison between flat surface and road surface

### 4.4.1 Rubber contact comparison on static condition

Contact area comparison intended to understand how the contact area vary due to rubber-wheel contact pairs. *Figure 4.29* displays the apparent contact condition between road surface and flat surface. The apparent contact area of road surface and flat surface were obtained through the calculation using Otsu thresholding formula. While the nominal contact area of rubber-wheel and road surface was procured based on the width of apparent contact area on road surface that covered with rubber-wheel multiple by rubber thickness. This nominal contact area on road surface was calculated to understand how deformed rubber-wheel on the road surface compare to the flat surface. The images show that the rubber deformation on road surface was larger than that on flat surface as the effect of small contact area. It is an indication that the roughness of mating surface affects the apparent contact area of rubber-wheel under same amount applied normal load. Consequently, it did not only affect the apparent contact area but also affected the deformation of rubber-wheel.

*Figure 4.30* shows the apparent contact area of rubber-wheel contact on road surface and flat surface in the influence of applied normal load. Although the amount of contact area differs significantly, the trendline of both curves show similar tendency where the apparent

contact area increased as applied normal load increased. Also, the increment of apparent contact area at higher applied normal load deteriorates in some degree. *Figure 4.31* shows the relationship between the apparent contact area ratio of road surface and flat surface under the effect of applied load.  As displayed in the graph, the ratio of road surface contact area and flat surface contact area was increased as applied normal load increased. However, at higher applied load the effect of normal load demised gradually. This result specifies the effect applied normal load more significant on road surface than that of flat surface. Similar result was also reported by Kenji Matsuda et.al. when they conducted experiment about the effect of specimen thickness on growth of real contact area of rubber with regular wavy surface [52].



Apparent contact area on road surface          Nominal contact area on road surface          Apparent contact area on flat surface
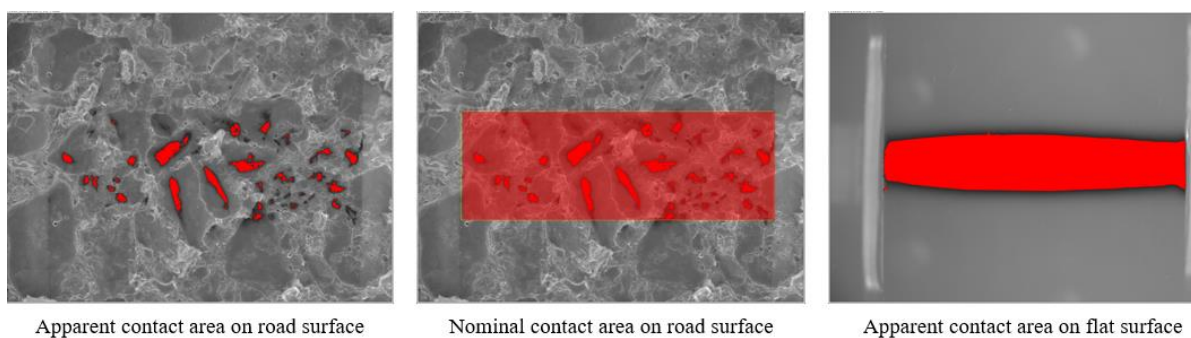
**Figure 4.29** Road surface contact area (apparent contact area and nominal contact area) and real contact area of flat surface under 40.2 N applied normal load
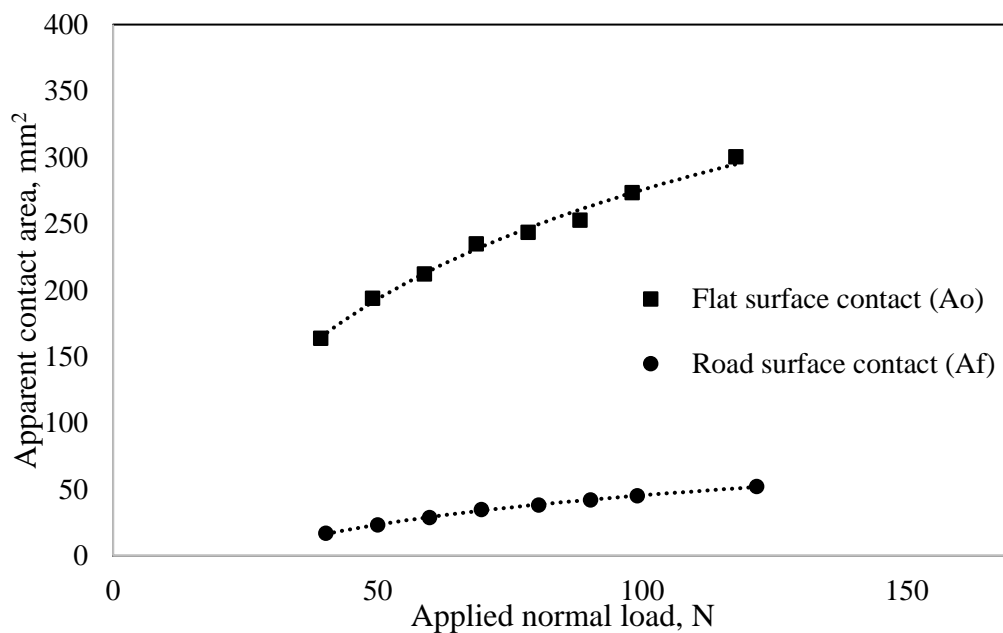


**Figure 4.30** Rubber-wheel apparent contact area due to applied load on both flat and road surfaces
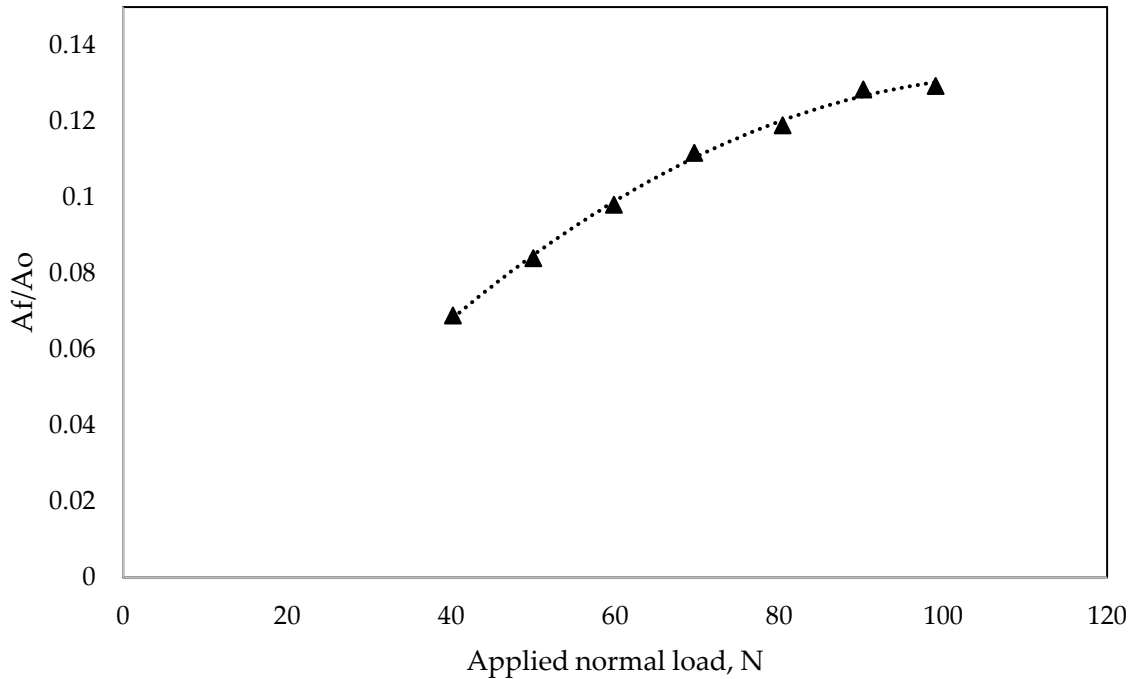
**Figure 4.31** Relationship between road surface/flat surface contact area ratio in the influence of applied normal load

**4.4.2** Rubber contact comparison on dynamic condition

*Figure 4.32* shows the relationship between rubber-wheel contact on road surface and flat surface on dynamic situation. The graph illustrates the ratio rubber contact on road surface and flat smooth surface due to the effect of moving speed under three type applied loads 40.2 N, 60.8 N and 80.4 N, respectively. Overall, the curves pattern shows decreasing trendline as moving speed increased. This result implies that the moving speed effect on rubber-wheel contact was more significant on smooth flat surface. The applied normal load effect on rubber-wheel contact ratio of road surface and smooth flat surface can be seen on the graph as applied load increased the contact ratio. However, the applied normal load 60.8 N and 80.4 N show similar amount tendency on ratio of rubber-wheel contact on road surface and smooth flat surface.
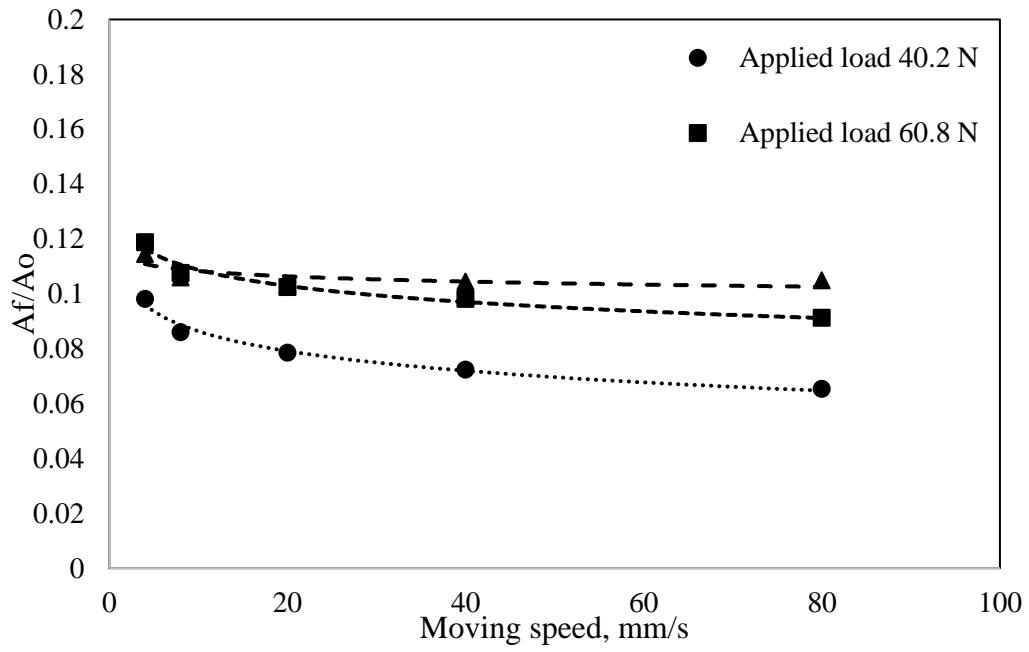
**Figure 4.32** Rubber-wheel contact ratio between road surface and flat surface

# Chapter 5 Conclusions

## 5.1 Summery

An ultraviolet-induced fluorescence technique using a pyranine solution was used to observe the contact condition between a cylindrical rubber-wheel and flat/road surfaces in situ. The purpose of this study is to determine applied load and moving speed dependencies on the contact area of rubber-wheel. The experiment was conducted in static and dynamic condition under wet surface simulating the situation of rainy season. The result obtained from the experiments can be conclude as follow:

### 5.1.1 Rubber-wheel contact on flat surface

The results of rubber-wheel contact area on smooth flat surface illustrating applied normal load dependency on the apparent contact area and the real contact area. The experiment on static condition carried out three times in order to obtained more accurate information. The contact area of rubber-wheel from three tests show that both the apparent contact area and the real contact area were increased as the applied load increased. In case of dynamic condition, there are different trendline can be observed at low and high moving speeds. At lower moving speed, the apparent and the real contact areas of rubber-wheel increased as moving speed increased up to 8 mm/s. At higher speed more than 8 mm/s, the apparent and the real contact areas of rubber-wheel reduced gradually as moving speed increased. The effect of applied load on dynamic condition can be seen as the fluctuation of both contact areas on higher applied were less than that on lower applied load.

### 5.1.2 Rubber-wheel contact on road surface

The effect of applied normal load on the apparent contact area between rubber-wheel and road surface in static test was similar to the contact area on smooth flat surface. The rise of the apparent contact area at lower applied loads was linear to applied normal load, and it was degraded at higher applied normal loads. In the dynamic condition test, the apparent contact area between the loaded rubber-wheel and road surface reduced as the moving speed increased. In all applied normal loads, it reduced significantly at speeds below 20 mm/s, and then continues to decrease gradually at higher speeds above 20 mm/s.

**5.1.3** Rubber contact comparison between road surface and smooth flat surface

The comparison rubber-wheel contact between smooth flat surface and road surface was investigated. The comparison was carried out on the apparent contact area. The apparent contact area of rubber-wheel on flat surface was larger than the apparent contact area of rubber-wheel on road surface. It is because the rubber-wheel only bumped with some protrusion parts of the road surface, not on the whole surface of the road. As a result, the pressure inside the rubber-wheel was higher that made the deformation larger on road surface. It can be seen on the nominal contact area on road surface was larger than that on smooth flat surface.

The results also display different rubber-wheel contact area tendency between road surface and smooth flat surface due to the effect of applied normal load and moving speed. The applied normal load influence on rubber-wheel contact on road surface was significant than that on smooth flat surface. However, moving speed influence on rubber-wheel contact on smooth flat surface was greater than it effect on road surface.

## 5.2 Limitation of observation method and suggestion for future works

Fluorescence microscopy is an excellence observation method in measuring contact area of mating surface. However, there are some external factors that affect greatly on measurement result needed to put into consideration. They are scattering light, reflection, and some others. Among them, the reflection on mating surface is the utmost problem in fluorescence microscopy, especially on rough mating surface like road surface. However, the influence of reflection was very minimum on smooth surface of mating contact. On the rough surface like road surface, the irregular pattern preventing us on finding the proper thresholding number for determining the boundary of real contact area even inside pressure contact. Therefore, we were unable to measure the real contact area between rubber-wheel and road surface on our experiment.

Consequently, for better study in the future, I strongly recommend studying more in detail about the effect of reflection on fluorescence microscopy before conducting experiment on rough mating surface. We need to conduct this research thoughtfully in order to solve the problem of reflection.

# References

[1] J. Winroth, W. Kropp, C. Hoever and P. Höstmad, "Contact stiffness considerations when simulating tyre/road noise," *Journal of Sound and Vibration,* vol. 409, pp. 274-286, 2017.

[2] M. Ilse, "Evaluation of tire/surfacing/base contact stresses and texture depth," *International Journal of Transportation Science and Technology,* vol. 4, no. 1, pp. 107-118, 2015.

[3] B. M. Redrouthu and S. Das, "Tyre modelling for rolling resistance," Master's thesis, 2014.

[4] G. Heinrich and M. Klüppel, "Rubber friction, tread deformation and tire traction," *Wear,* vol. 265, no. 7-8, pp. 1052-1060, 2008.

[5] e. c. Michelin, "The Tyre: Grip," Société de technologie Michelin, 2001.

[6] K. Holmberg, P. Andersson and A. Erdemir, "Global energy consumption due to friction in passenger cars," *Tribology international,* vol. 47, pp. 221-234, 2012.

[7] K. Akutagawa, "Technology for reducing tire rolling resistance," *Tribology Online,* vol. 12, no. 3, pp. 99-102, 2017.

[8] M. Chandrasekaran and A. W. Batchelor, "In situ observation of sliding wear tests of butyl rubber in the presence of lubricants in an X-ray microfocus instrument," *Wear,* vol. 1, no. 35-43, p. 211, 1997.

[9] I. Nitta, R. Ebuchi, Y. Yasuda and H. Terao, "Observation of real contact area using laser microscope with wide field of view," *Journal of Advanced Mechanical Design, Systems, and Manufacturing,* vol. 3, no. 150-159, p. 5, 2011.

[10] N. Marx, J. Guegan and H. A. Spikes, "Elastohydrodynamic film thickness of soft EHL contacts using optical interferometry," *Tribology International,* vol. 99, pp. 267-277, 2016.

[11] J. H. H. Bongaerts, J. P. R. Day, C. Marriott, P. D. A. Pudney and A. M. Williamson, "In situ confocal Raman spectroscopy of lubricants in a soft elastohydrodynamic tribological contact," *Journal of Applied Physics,* vol. 104, no. 1, p. 014913, 2008.

[12] M. T. Fowell, C. Myant, H. A. Spikes and A. Kadiric, "A study of lubricant film thickness in compliant contacts of elastomeric seal materials using a laser induced fluorescence technique," *Tribology International,* vol. 80, pp. 76-89, 2014.

[13] L. Ma and C. Zhang, "Discussion on the technique of relative optical interference intensity for the measurement of lubricant film thickness," *Tribology letters,* vol. 36, no. 3, p. 239, 2009.

[14] A. E. Smart and R. A. J. Ford, "Measurement of thin liquid films by a fluorescence technique," *Wear,* vol. 29, no. 1, pp. 41-47, 1974.

[15] R. A. J. Ford and C. A. Foord, "Laser-based fluorescence techniques for measuring thin liquid films," *Wear,* vol. 51, no. 2, pp. 289-297, 1978.

[16] B. Liu, Y. Shen, H. Zhang, C. Liu, Z. Tang and X. Yuan, "Visualization of structured packing with laser induced fluorescence technique: Two-dimensional measurement of liquid concentration distribution.," *Transactions of Tianjin University,* vol. 22, no. 5, pp. 466-472, 2016.

[17] W. E. DeVinney, "Factors Affecting Tire Traction," *SAE Transactions,* pp. 1649-1656, 1968.

[18] J. D. Kelley Jr, "Factors Affecting Passenger Tire Traction on the Wet Road," *SAE Transactions,* pp. 580-592, 1968.

[19] B. Zheng, X. Huang, W. Zhang, R. Zhao and S. Zhu, "Adhesion Characteristics of Tire-Asphalt Pavement Interface Based on a Proposed Tire Hydroplaning Model," *Advances in Materials Science and Engineering,* pp. 1-12, 2018.

[20] H. Hertz, "Ueber die Berührung fester elastischer Körper," *Journal für die reine und angewandte Mathematik,* no. 92, pp. 156-171, 1882.

[21] J. F. Archard, "Elastic deformation and the laws of friction," in *Proceedings of the Royal Society of London. Series A. Mathematical and Physical Sciences*, 1957.

[22] D. Tabor, The hardness of metals, Oxford University press, 2000.

[23] J. A. Greenwood and J. P. Williamson, "Contact of nominally flat surfaces," in *Proceedings of the royal society of London. Series A. Mathematical and physical sciences*, 1966.

[24] B. V. Derjaguin, V. M. Muller and Y. P. Toporov, "Effect of contact deformations on the adhesion of particles," *Journal of Colloid and interface science,* vol. 53, no. 2, pp. 314-326, 1975.

[25] K. L. Johnson, Contact mechanics, Cambridge university press, 1987.

[26] K. L. Johnson, K. Kendall and A. Roberts, "Surface energy and the contact of elastic solids," in *Proceedings of the royal society of London. A. mathematical and physical sciences*, 1971.

[27] B. J. Hamrock, B. J. Schmid and B. O. Jacobson, Fundamentals of fluid film lubrication, CRC press, 2004.

[28] G. G. Stokes, "XXX. On the change of refrangibility of light," *Philosophical transactions of the Royal Society of London,* vol. 142, pp. 463-562, 1852.

[29] R. P. Haugland, Handbook of fluorescent probes and research chemicals, 8 ed., Molecular Probes, Eugene, 1996.

[30] "https://www.thermofisher.com," Thermo Fisher Scientific, [Online]. Available: https://www.thermofisher.com/jp/en/home/life-science/cell-analysis/cell-analysis-learning-center/molecular-probes-school-of-fluorescence/imaging-basics/fundamentals-of-fluorescence-microscopy/physical-properties-that-define-fluorescence.html. [Accessed 19 11 2020].

[31] R. Barnadas-Rodríguez and J. Estelrich, "Effect of salts on the excited state of pyranine as determined by steady-state fluorescence," *Journal of Photochemistry and Photobiology A: Chemistry,* vol. 198, no. 2-3, pp. 262-267, 2008.

[32] H. Inagaki, A. Saito, M. Murakami and T. Konomi, "Measurement of oil film thickness distribution on piston surface using the fluorescence method: development of measurement system," *JSME International Journal Series B Fluids and Thermal Engineering,* vol. 40, no. 3, pp. 487-493, 1997.

[33] W. J. Tango, J. K. Link and R. N. Zare, "Spectroscopy of K2 Using Laser-Induced Fluorescence," *The Journal of Chemical Physics,* vol. 49, no. 10, pp. 4264-4268, 1968.

[34] "https://www.olympus-lifescience.com," [Online]. Available: https://www.olympus-lifescience.com/es/microscope-resource/primer/techniques/fluorescence/filters/. [Accessed 19 11 2020].

[35] R. C. Gonzalez and R. E. Woods, Digital Image processing, 4th ed., New York: Pearson Education, 2018.

[36] S. Sarkar, S. Das and S. S. Chaudhuri, "A multilevel color image thresholding scheme based on minimum cross entropy and differential evolution," *Pattern Recognition Letters,* vol. 54, pp. 27-35, 2015.

[37] Q. Miao, P. Xu, T. Liu, J. Song and X. Chen, "A novel fast image segmentation algorithm for large topographic maps," *Neurocomputing,* vol. 168, pp. 808-822, 2015.

[38] A. K. Bhandari, A. Kumar and G. K. Singh, "Tsallis entropy based multilevel thresholding for colored satellite image segmentation using evolutionary algorithms," *Expert systems with applications,* vol. 42, no. 22, pp. 8707-8730, 2015.

[39] E. Smistad, T. L. Falch, M. Bozorgi, A. C. Elster and F. Lindseth, "Medical image segmentation on GPUs–A comprehensive review," *Medical image analysis,* vol. 20, no. 1, pp. 1-18, 2015.

[40] D. Petrova, B. Weber, C. Allain, P. Audebert, C. H. Venner, A. M. Brouwer and D. Bonn, "Fluorescence microscopy visualization of the roughness-induced transition between lubrication regimes," *Science advances,* vol. 5, no. 12, p. eaaw4761, 2019.

[41] N. Otsu, "A threshold selection method from gray-level histograms," *IEEE transactions on systems, man, and cybernetics,* vol. 9, no. 1, pp. 62-66, 1979.

[42] S. I. Syafi'i, R. T. Wahyuningrum and A. Muntasa, "Segmentasi Obyek Pada Citra Digital Menggunakan Metode Otsu Thresholding," *Jurnal Informatika,* vol. 13, no. 1, pp. 1-8, 2015.

[43] "https://www.ditect.co.jp," DITECT, Digital Image Technology, [Online]. Available: https://www.ditect.co.jp/en/camera/has_u2.html. [Accessed 19 11 2020].

[44] Y. Avnir and Y. Barenholz, "pH determination by pyranine: medium-related artifacts and their correction," *Analytical biochemistry,* vol. 347, no. 1, pp. 34-41, 2005.

[45] H. Zhu, R. C. Derksen, C. R. Krause, R. D. Fox, R. D. Brazee and H. E. Ozkan, "Fluorescent intensity of dye solutions under different pH conditions," *Journal of ASTM international,* vol. 2, no. 6, pp. 1-7, 2005.

[46] J. Santana, K. R. Perez, T. B. Pisco, D. D. Pavanelli, D. Briotto Filho, D. Rezende and L. F. Gomes, "A high sensitive ion pairing probe (the interaction of pyrenetetrasulphonate and methyl viologen): Salt and temperature dependences and applications," *Journal of Luminescence,* vol. 151, pp. 130-137, 2014.

[47] S. Maegawa, F. Itoigawa and T. Nakamura, "Optical measurements of real contact area and tangential contact stiffness in rough contact interface between an adhesive soft elastomer and a glass plate," *Journal of Advanced Mechanical Design, Systems, and Manufacturing,* vol. 9, no. 5, pp. JAMDSM0069-JAMDSM0069, 2015.

[48] A. J. Bur, M. G. Vangel and S. Roth, "Temperature dependence of fluorescent probes for applications to polymer materials processing," *Applied Spectroscopy,* vol. 56, no. 2, pp. 174-181, 2002.

[49] "https://docs.opencv.org," OpenCV , [Online]. Available: https://docs.opencv.org/master/d7/d4d/tutorial_py_thresholding.html. [Accessed 3. 9. 2020].

[50] J. Rahman, T. Iwai, K. Koshiba and Y. Shoukaku, "Observation of contact area of rubber wheel using an ultraviolet-induced fluorescence method," in *Asia International Conference on Tribology*, Serawak, 2018.

[51] M. Kluppel, A. Muller, A. Le Gal and G. Heinrich, "Dynamic contact of tires with road tracks," in *2003 Technical Meeting of the American Chemical Society, Rubber Division*, 2003.

[52] K. Matsuda, S. Mori, A. Hatanaka, T. Sunahara and K. Nakamura, "Effect of specimen thickness on growth of real contact area of rubber with two-dimensional regular wavy surface," *Tribology International,* vol. 124, pp. 184-194, 2018.